SANDIA REPORT
SAND2024-15020
Printed September 2023

Sandia National Laboratories

Investigation of SF6 Alternatives in Spark Gap Switches for GWP Reduction

Marc D. Mitchell, Adam M. Steiner, Matthew L. Burnette, Max C. Flynn, Joseph Felix, Matthew M. Hopkins, Andy M. Castillo, Amanda M. Lietz, Jacob C. Stephens

Prepared by
Sandia National Laboratories
Albuquerque, New Mexico
87185 and Livermore,
California 94550

Issued by Sandia National Laboratories, operated for the United States Department of Energy by National Technology & Engineering Solutions of Sandia, LLC.

Available to DOE and DOE contractors from
U.S. Department of Energy
Office of Scientific and Technical Information
P.O. Box 62
Oak Ridge, TN 37831

Telephone: (865) 576-8401
Facsimile: (865) 576-5728
E-Mail: reports@osti.gov
Online ordering: http://www.osti.gov/scitech

Available to the public from
U.S. Department of Commerce
National Technical Information Service
5301 Shawnee Rd
Alexandria, VA 22312

Telephone: (800) 553-6847
Facsimile: (703) 605-6900
E-Mail: orders@ntis.gov
Online order: https://classic.ntis.gov/help/order-methods/

ABSTRACT

This primary purpose of this project was to evaluate alternative gas mixtures to sulfur hexafluoride (SF6) developed for high voltage power delivery applications for use in high voltage spark gap switches. These SF6 alternatives lower global warming potential emissions and enable improvements to the pressure-voltage design space. A combined experimental, computational, and theoretical study was used to quantify the impact of persistent breakdown products on the breakdown distribution of SF6-replacement gas mixtures. Viable SF6 replacements suitable for use in spark gap switches were studied to enable performance and agility improvements for next-generation pulsed power research relevant to national security missions. Experimental campaign included establishing parameters of switch gases as function of concentration. Various concentrations and pressures were tested for trends in breakdown voltage, repeatability, and durability, and breakdown constituents. A zero-dimensional plasma global model was used to simulate the plasma arc decay and recombination process in spark-gap switches relevant to the Z machine. Finally, a complete and consistent set of electron-neutral collision cross-sections for the novel insulating gas C4F7N is reported.

ACKNOWLEDGEMENTS

Karen DeZetter

Lucas Muller

Allen Crabtree

Brian Stoltzfus

CONTENTS

LIST OF FIGURES

LIST OF TABLES

This page left blank

ACRONYMS AND TERMS

Acronym/Term	Definition
NGPP	Next generation pulsed power
Novec or Novec-4710	Trade name for C_4F_7N
RR	Radio frequency
GWP	Global warming potential
kV	kilovolt
TTU	Texas Tech University
mJ	Millijoules
MTG	Marx trigger generator
RGA	Residual gas analyzer
M/Q	Mass per charge

1. INTRODUCTION

1.1. Project Motivation

Sulfur hexafluoride (SF_6) is presently the gas of choice in high voltage spark-gap switches, which are an integral part of large pulsed power systems such as Z, Saturn, and Hermes III at Sandia National Laboratories. While SF_6 has favorable properties for spark-gap operation, the environmental consequences of a release of SF_6 are significant. SF_6 is an extremely potent greenhouse gas, and Sandia accounts for a substantial fraction of the SF_6 used in the DoE complex, with Z, Saturn, and Hermes III together accounting for about a third of the total greenhouse gas emissions of the Sandia New Mexico site. With no improvements to present operating conditions, a proposed next generation pulsed power (NGPP) facility could release up to ten times the amount of SF_6 compared to the Z facility. Identifying a viable alternative switch gas for next-generation pulsed power systems would lower our environmental impact and increase confidence in our ability to comply with future regulatory requirements. This repot describes the results of an experimental, theoretical, and computational study of several gas mixtures based on Novec-4710 to evaluate breakdown statistics, persistent byproduct formation, and dielectric strength retention in spark gap environments.

Spark gap gas switches are ubiquitous on large pulsed power systems due to their unique capability to switch currents in the hundreds of kiloamps while holding off voltages in the megavolts. Switches operating in this regime typically utilize SF_6 as the insulating medium because its high breakdown voltage and electron affinity allow for well-controlled triggered breakdown while resisting unintended breakdown at relatively modest pressures. Because SF_6 is among the most potent greenhouse gases, with a global warming potential (GWP) over 23,000 times larger than carbon dioxide (CO_2), alternatives to SF_6 with lower GWP have been developed for many high voltage insulation applications, including live-tank circuit breakers, gas-insulated substations, and gas insulated transmission lines.

Prior research involving g^3 and AirPlus has shown promising results in reproducing the dielectric strength, arc quenching potential, and recoverability after arcing of SF_6 under discharge conditions in high-voltage switchgear, leading to the development of commercial switchgear products [1]. Additionally, 200-kV spark gaps utilizing a similar mixture to g^3 have been shown to outperform dry air and perform comparably to SF_6 in terms of breakdown voltage stability of fresh (previously unarced) gas [2]. However, little information exists on breakdown products in spark gap-relevant discharge conditions and their impacts on reliability and lifetime. The impact of a reliable high-performance spark gap switch using one of the SF_6 replacement mixtures would be transformative to pulsed power, dramatically reducing the GWP inventory required to operate spark gap switches while potentially reducing the operating pressures or switch inductances necessary for voltage holdoff.

Existing SF_6 alternatives for high voltage switchgear primarily utilize 3M Novec 4710, a fluronitrile (C_4F_7N), also called C4; or 3M Novec 5110, a fluoroketone ($C_5F_{10}O$), also called C5. These gases both have high breakdown voltages and are typically diluted with CO_2 or dry air to increase thermal stability and (in the case of C4) lower the overall GWP [4-5]. Previous computational and experimental studies have examined the breakdown kinetics of these fluorinated gases [6-9] or the diluted mixtures [10-12] and their interactions with solid electrodes [13-14] under thermal, RF, or pulsed electrical decomposition. A recent study also compared the self-breakdown distribution of C_4F_7N/N_2 with SF_6/N_2 in a switch designed for a linear transformer driver, although no comparison was made to pure SF_6. Our approach differs from previous work in that we are investigating how the breakdown distribution changes after the gas chemistry has been altered by electrical energy

dissipated in the switch, typical of capacitive discharges on large pulsed power systems. Understanding permanent or slowly reversing changes in gas chemistry and their effect on switch performance is crucial to establishing the viability of a proposed alternative to eventually replace SF_6 in large pulsed power systems.

1.2. Project Approach

In this study, we evaluated replacement gas mixtures for SF6 for spark gap switch applications, which differ substantially from existing insulating applications in that electrical breakdown events in spark gaps are desired, frequent, and numerous, but tend to dissipate much lower specific energies compared to unintended arc discharges in power distribution equipment. Through a combination of experimental, theoretical, and computational investigation, we measured the effects of energetic discharges on the breakdown distribution of candidate SF6 replacement gas mixtures, determined persistent breakdown products and their effects on the chemical makeup of arced gas, and compared with kinetic breakdown models. Our hypothesized improvement over the state of the art, pure SF6, is at least a factor of 100 reduction in required GWP inventory while maintaining or exceeding the performance of SF6 in terms of mean breakdown voltage, standard deviation of breakdown voltage, and jitter of triggered breakdown timing.

Experiments were conducted on Switch-A-Roo, an existing test stand which has been operated by 1650 personnel for spark gap research and development, using L3 T-670 switches. Gas mixtures tested included Novec-4710/O2/CO2 in a 4/10/86 molecular ratio, Novec-4710/CO2 in a 4/96 ratio, pure SF6, and SF6/N2 in a 10/90 molecular ratio. Self-break voltage distributions were recorded, and a differentially pumped mass spectroscopy apparatus was developed and fielded in situ on Switch-A-Roo to examine byproduct gases at times ranging immediately after breakdown up to 24 hours after breakdown. For each gas, a series of experiments were conducted to:

1. Determine the initial self-breakdown threshold statistical distribution for each tested gas mixture;
2. Determine the gas composition after energetic discharges, varying the number of consecutive discharges and elapsed time before mass spectroscopy measurement; and
3. Determine the changes to the breakdown distribution after triggered discharges typical of a spark gap operation on a pulsed power system between gas purges.

These data were compared with global and fluid models of gas breakdown chemical kinetics to increase confidence in predicting breakdown product formation and effects at higher voltage and deposited energies.

1.3. Project Components

This project included parallel experimental, theoretical, and computational components in order to characterize and predict the viability of insulating gas mixtures in spark gap switches. These components will be reported in 4 different parts as follows:

1. Experimental Breakdown Distribution (SNL): Establish parameters of switch gases as function of concentration, testing various gas compositions non-perturbatively for trends in breakdown voltage, before and after energetic discharge events. Results from these experiments are presented in Section **Error! Reference source not found.**.

Commented [SAM1]: We didn't meet this because we used a 4% mixture (with GWP 85) which had about half the strength of SF6. A 10% mixture probably matches the strength of SF6 but we haven't tested it yet because it arrived on Monday. The 10% mixture would meet our requirements with a GWP of 210 which just squeaks in the factor of 100x reduction

Commented [SAM2]: I don't know why it's not Switcheroo but this is the actual spelling on documentation for the system

2. Experimental Gas Chemistry via RGA (SNL): Study persistent changes in gas composition using a residual gas analyzer (RGA). Results from these experiments are presented in Section **Error! Reference source not found.**.
3. Plasma Chemistry Modeling of Novec 4710 (SNL): Assemble reaction mechanisms for mixtures containing C_4F_7N studied on Switch-A-Roo, use the global model to determine breakdown products as a function of electrical action and/or deposited energy, and compare output with measurements from RGA study. Results from this study are presented in Section **Error! Reference source not found.**.
4. Generation and optimization of cross-sections for electron-C_4F_7N collisions (TTU): Calculate the ionization coefficient and electron transport properties using a multi-term model and use these results to deduce breakdown voltage as a function of gap spacing and pressure via the application of an appropriate streamer-Paschen breakdown model. Results from this study are presented in Section **Error! Reference source not found.**.

2. EXPERIMENTAL BREAKDOWN DISTRIBUTION

Experiments were conducted on Switch-A-Roo, a spark gap test stand located in the Pulsed Power Component Development Laboratory (PPCDL), originally designed for evaluating breakdown distribution and switch jitter in linear transformer driver bricks. Gas mixtures evaluated included:

- Synthetic dry air (Matheson Ultra Zero)
- Pure SF_6
- SF_6/N_2 with 10/90 molecular ratio
- $C_4F_7N/O_2/CO_2$ with 4/10/86 molecular ratio
- C_4F_7N/CO_2 with 4/96 molecular ratio

Tests were also attempted with pure C_4F_7N; however, it was found that the pure fluoronitrile gas would not break down at the maximum rated voltage of the T670 switch at gauge pressures as low as 0.5 psi.

2.1. Experimental Setup

Switch-A-Roo is an automated system that applies a stepped DC voltage waveform until a breakdown event is detected (Figure 2.1). The system consists of an oil tank where the switch and any high voltage components are contained. Two Spellman SL300 power supplies are controlled via software to apply 1 kV steps very 0.5 s (Figure 2.2). Ballast resistors (5 kΩ water resistors) are placed in series between the power supplies and the switch. Optional 20 nF capacitors can be installed in parallel between the switch electrodes and ground to vary the amount of energy available for the switch. Inclusion of these capacitors allows for a high energy discharge mode, which deposits up to 10 J in the switch for the maximum 100 kV applied differential voltage, as estimated from circuit simulations of spark gap channels using the method of Pouncey [16] updated with the T. H. Martin-Braginskii model of switch conductivity [14, 15] . The low-energy discharge mode without the capacitors disconnected deposits only the energy in the arc associated with the stray capacitance of the electrodes (along with a small contribution from the power supply output capacitance and cable capacitance, resistively divided between the switch arc and the 5 kΩ ballast resistors); this energy is approximately 10 mJ.

The switch used is a modified L3 T-670 field distortion switch, modified to include an SNL-designed trigger plane and electrodes to match those currently used on the Z Marx trigger generators (MTGs). The midplane of the switch is connected to ground via a 10 kΩ water resistor. A schematic of the system is shown in Figure 2.3. A Fluke 717-100G meter is used to measure the gas pressure before and after a sequence of shots.

Commented [SAM3]: There's a reference problem, and also it's probably better to reorder the figures in the order they are mentioned in the text

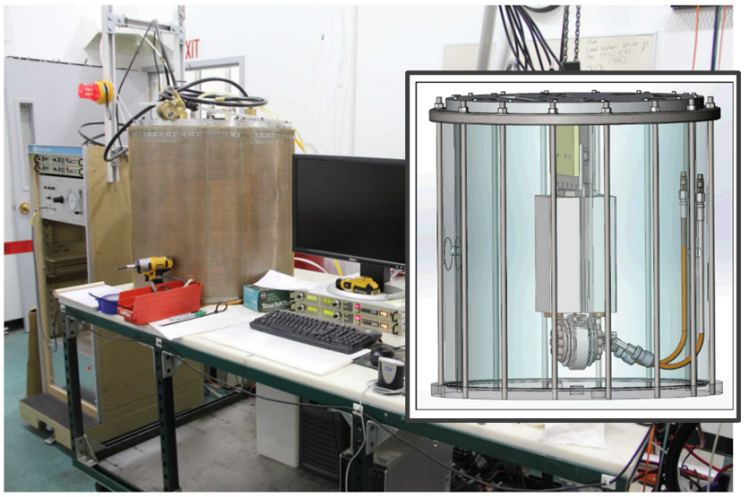

Figure 2.1. Switch-a-roo test bed

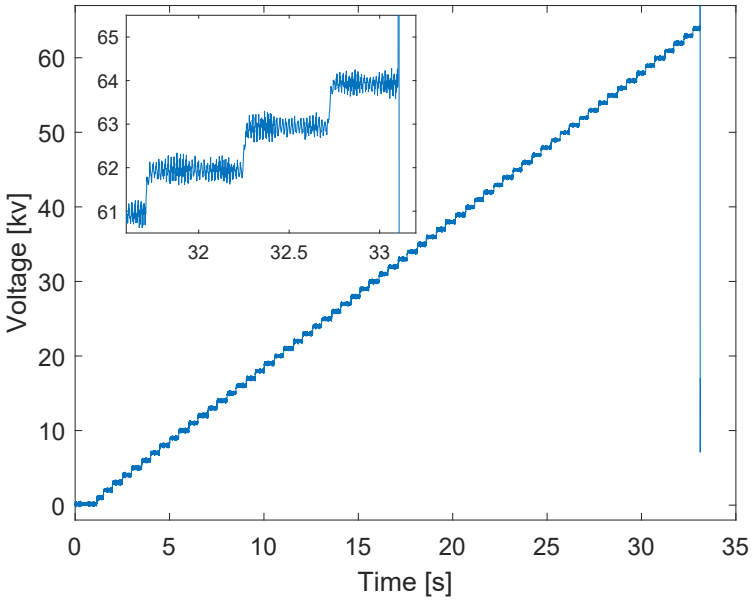

Figure 2.2. Example voltage waveform with inset showing the final steps before self-break

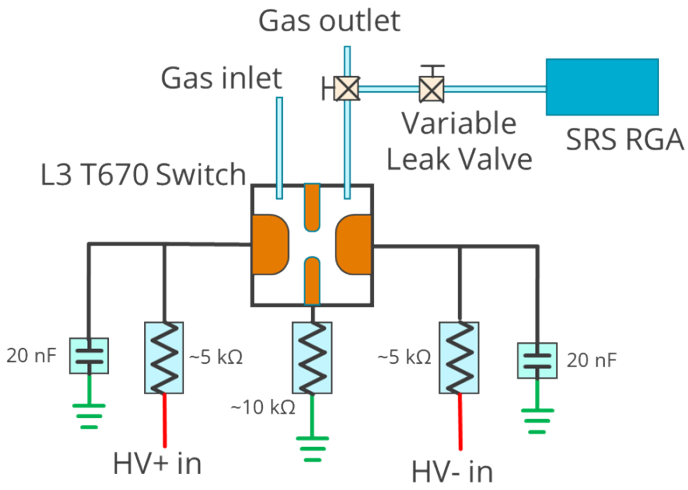

Figure 2.3. Schematic of the Switch-a-roo test bed

2.2. Experimental Procedure

The test procedure began with installing a cleaned switch with new electrode hardware. The gas was evacuated through a reclaimer and fresh gas was flowed into the switch. The switch was conditioned using 25 shots at increasing pressures. This was repeated four more times for a total of 625 shots. The last 125 shots at 5 different pressure steps were used to generate a linear Paschen breakdown curve for the self-break voltage of the switch. An example linear Paschen fit to the data is shown in Figure 2.4. This allowed for determining the nominal self-break voltage at a given pressure.

After break-in of the switch electrodes, the following steps were performed to gather both RGA data on breakdown products (see Section **Error! Reference source not found.**) and breakdown distribution measurements. Before each step, gas from the previous step was reclaimed and new gas was supplied from the bottle.

1. Collect an initial 500-shot breakdown distribution (the baseline case) in the low-energy mode.
2. Measure the baseline gas composition on the RGA, continuously scanning (~2-3 minutes per scan) over 24 hours.
3. Conduct 1 high energy shot at nominal 100 kV breakdown (~10 J), then measure the gas composition on the RGA, continuously scanning over 24 hours.
4. Conduct 3 high energy shots at nominal 100 kV breakdown (~30 J), then measure the gas composition on the RGA, continuously scanning over 24 hours.
5. Conduct 5 high energy shot at nominal 100 kV breakdown (~50 J), then measure the gas composition on the RGA, continuously scanning over 24 hours.
6. Conduct 10 high energy shots at nominal 100 kV breakdown (~100 J), then measure the gas composition on the RGA, continuously scanning over 24 hours.

7. Conduct 1 high energy shot at nominal 100 kV breakdown (~10 J), then collect a 500-shot breakdown distribution.
8. Conduct 3 high energy shots at nominal 100 kV breakdown (~30 J), then collect a 500-shot breakdown distribution.
9. Conduct 5 high energy shots at nominal 100 kV breakdown (~50 J), then collect a 500-shot breakdown distribution.
10. Conduct 10 high energy shots at nominal 100 kV breakdown (~100 J), then collect a 500-shot breakdown distribution.

For some gas mixtures, additional tests were performed after step 10, including collecting breakdown distributions for order 100 shots in the high energy mode, and performing triggered breakdown shots at self-break fractions ranging from 60-90%, then collecting a breakdown distribution in the low-energy mode.

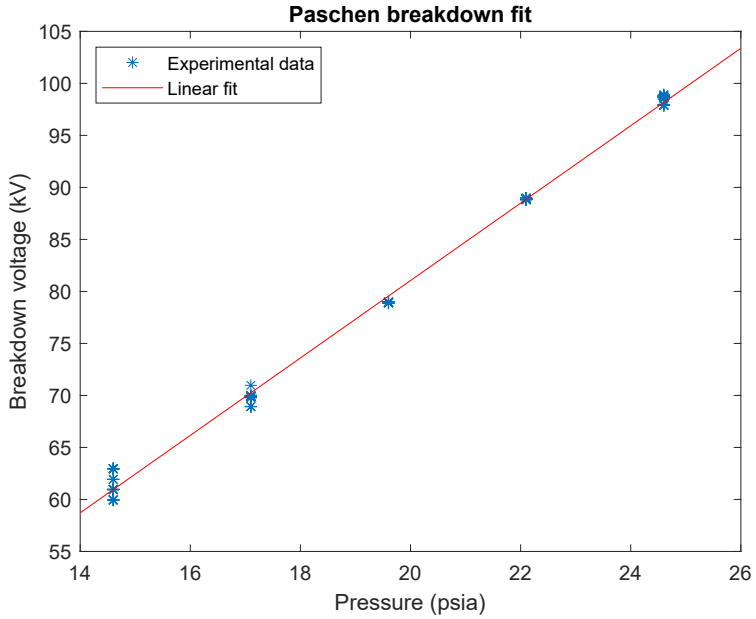

Figure 2.4. Linear Paschen fit to breakdown data for pure SF_6 on a T670 switch after break-in.

2.3. Novec 4710 Material Incompatibility

During the first attempt to collect data using a Novec 4710 mixture, a slow leak was noted which grew with time until it became so large that further experiments were not possible. Careful tests on all exterior-facing system components were performed, but no leaks to the environment were discovered. Upon further investigation, it was found that the mixture was attacking the Teflon seals in Swagelok ball valves, and the gas was leaking through the valves into the vacuum apparatus used for RGA measurements. The system was redesigned using with certified Novec-compatible parts purchased from DILO. A small number of NPT fittings were required to converted from the DILO

hardware to the insulating tubes feeding the switch (because the switch handles high voltage, it is not possible to field a gas system with metal-only lines all the way to the spark gap). The NPT fittings were sealed with SWAK, which was sufficient to eliminate or reduce the leak rate below the measurement threshold over the course of the 24-hour tests described in Section 2.2.

Unfortunately, the Fluke 717-100G meter was also noted to leak internally after exposure to Novec. Because we required a precise measurement of gas pressure to detect order 1% changes in breakdown voltage (i.e. a greater precision than available through other digital pressure transducers fielded on the system), the Fluke gauge measurement technique was modified to avoid having the gauge connected during the 24-hour test durations. The gauge was isolated from the primary Novec-containing gas line and connected downstream of an isolation valve so that the gas could be vented after measuring the pressure. After running a sequence, the valve was opened, connecting the Fluke meter for a final pressure measurement, P_m. The true final pressure in the gas switch, P_{1f}, was found using the ideal gas law combining the gas switch volume (volume 1) and the small volume of the Fluke meter and feed lines (volume 2) assuming constant temperature as follows:

$$PV = nRT$$

$$P_m(V_1 + V_2) = (n_1 + n_2)RT$$

$$P_m(V_1 + V_2) = P_{1f}V_1 + P_{2f}V_2$$

$$P_{1f} = P_m + V_2/V_1(P_m + P_{2f})$$

A test fill of the Fluke meter region using dry air allowed for the direct measurement of the quantity V_2/V_1.

2.4. Experimental Results

Over the 500 shots for a given shot sequence, the pressure in the switch could vary due to a variety of factors including temperature changes, changing composition of the gas, and leaks. As a result, instead of plotting the measured breakdown voltages, the percent of self-break is reported instead. The percent of self-break is found by correcting the pressure assuming a linear change in pressure from the initial pressure before testing to the final pressure measured after running the shot sequence. Specifically, the percent of self-break $sb\%$ is found by the equation:

$$sb\% = 100\frac{V_{br}}{V_{sb}}$$

where V_{br} is the measured breakdown voltage and V_{sb} is the nominal self-break calculated from the Paschen curve, measured as in Section 2.2.

The results of the 500-shot baseline breakdown distributions for each gas is in Figure 2.5 along with quantile-quantile plots from the best fit Weibull distribution for each sequence. Results for the 500-shot breakdown distributions after 1, 3, 5, and 10 high energy shots are shown in Figure 2.6, Figure 2.7, Figure 2.8, and Figure 2.9, respectively. The results are summarized in

Table 2.1. In general, the data sets are plotted from 95% to 105% of nominal self-break for easy comparison across the data sets; however, data sets that exceeds this range are instead plotted such that all data fits in the plot range. The stair-stepping present in the data is a consequence of the

discrete breakdown voltage conditions on the Switch-A-Roo setup. In the low-energy configuration, the capacitance charged by the power supply (the stray capacitance of the switch gaps and the parallel capacitance of the cables) is so low that the minimum power supply output current cannot maintain a charge rate of 0.5 kV/s per polarity; therefore, the power supply outputs a several-ms burst of current, followed by a nearly 1-s hold at an integer differential voltage. The probability of breakdown is significantly larger on these voltage "stair steps" rather than during the fast rise between steps. We also note that the slight sloped features are due to pressure corrections, where pressure is fit to a linear function bounded by measurements immediately before and immediately after the 500-shot sequence.

The SF_6 baseline had the tightest distribution of all tests; however, with increasing energy deposition into the gas the distribution widened, and the occurrence of low voltage dropouts increased. Similar behavior was noted for the SF_6/N_2 mixture, though no dropouts below 95% of nominal self-break were noted up to 3 high energy shots. For the low voltage tail of the breakdown distribution, SF6 is consistently below the expected values, thus lower dropouts than predicted by a Weibull distribution are occurring. Interestingly, this is not the case for the SF_6/N_2 mixture, where the Weibull distribution is a conservative fit for the low voltage tail of the distribution.

The Novec $C4/O_2/CO_2$ mixture only had four shots below 95% of self-break; two occurred during the baseline distribution and two after 1 high energy shot of energy deposition. All four low self-breaks were just under 95%. The Novec $C4/CO_2$ mixture also only had four shots below 95% of self-break; all occurred after 10 high energy shots in succession from each other. These were the lowest self-breaks noted in all of this testing, being as low as 73.3% of self-break. There was no consistency in either Novec C4 mixture across all data sets for the Weibull fitting being a conservative or non-conservative fit for the low voltage tail of the distribution.

This testing suggests that the Novec C4 mixtures are a viable option to replace SF6 in low energy (up to 100 J) switching applications. The Novec $C4/O_2/CO_2$ mixture in particular showed a lower rate of low voltage dropouts, and the dropouts were not as severe as SF6.

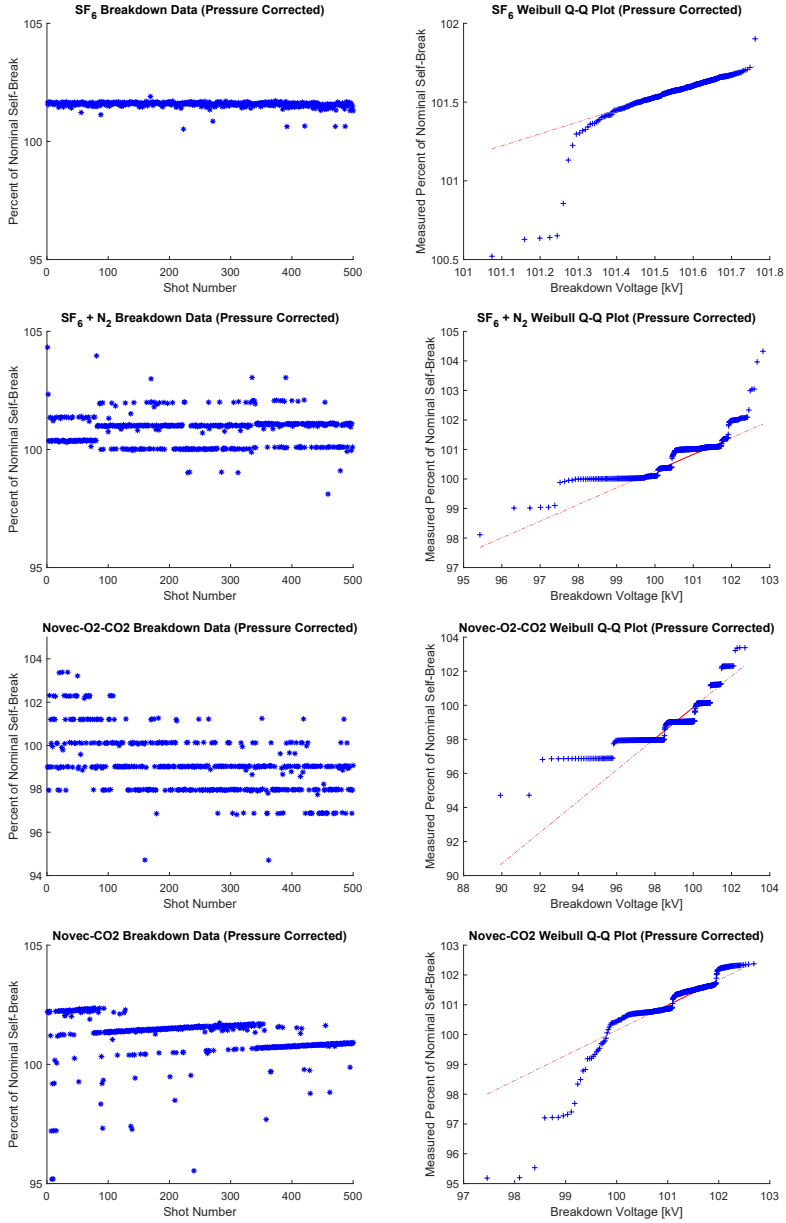

Figure 2.5. Baseline shots for the various gases. The left column is the 500-shot sequence; the right column is that data fit to a Weibull distribution.

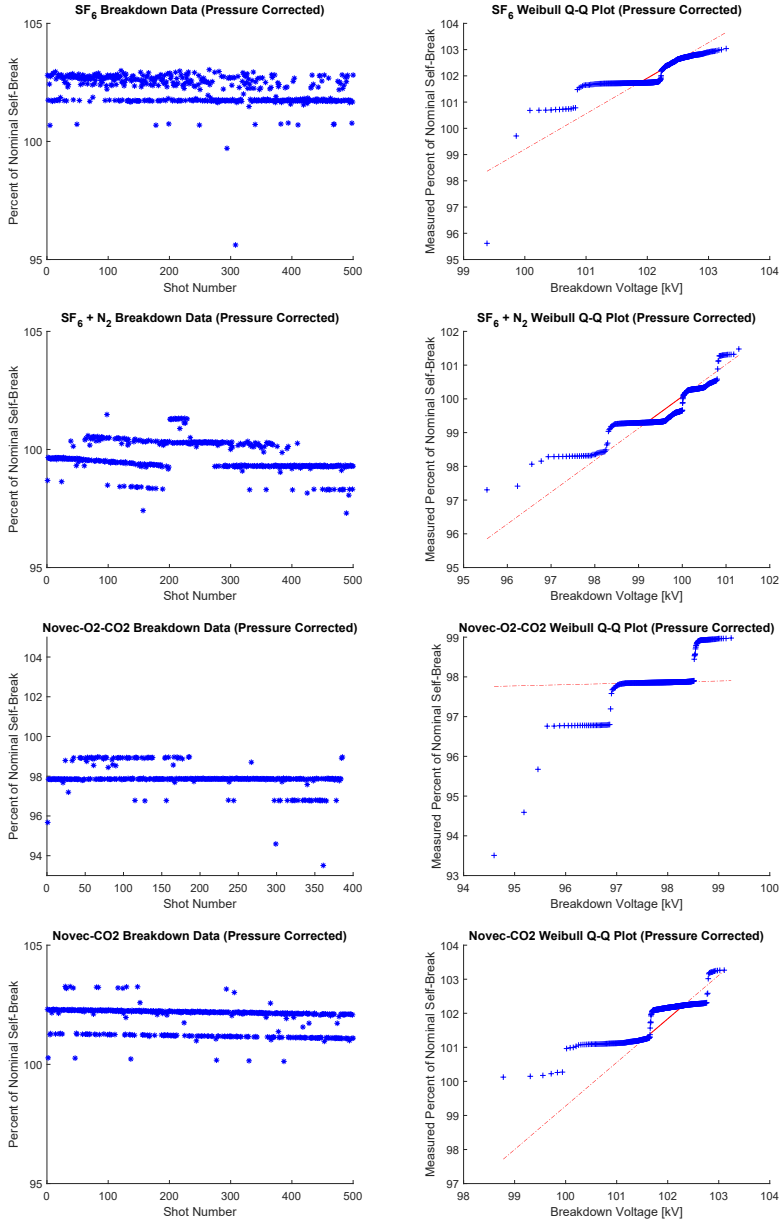

Figure 2.6. Post 1 high-energy shot for the various gases. The left column is the 500-shot sequence; the right column is that data fit to a Weibull distribution.

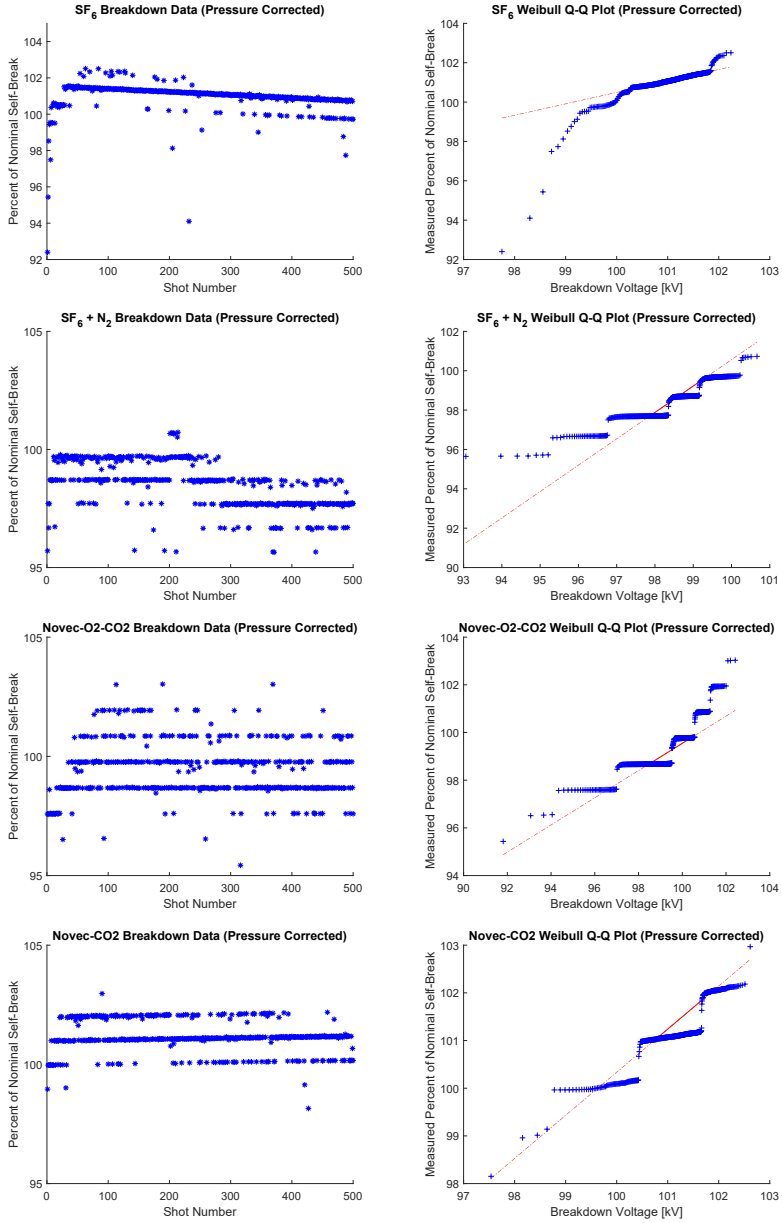

Figure 2.7. Post 3 high-energy shots for the various gases. The left column is the 500-shot sequence; the right column is that data fit to a Weibull distribution.

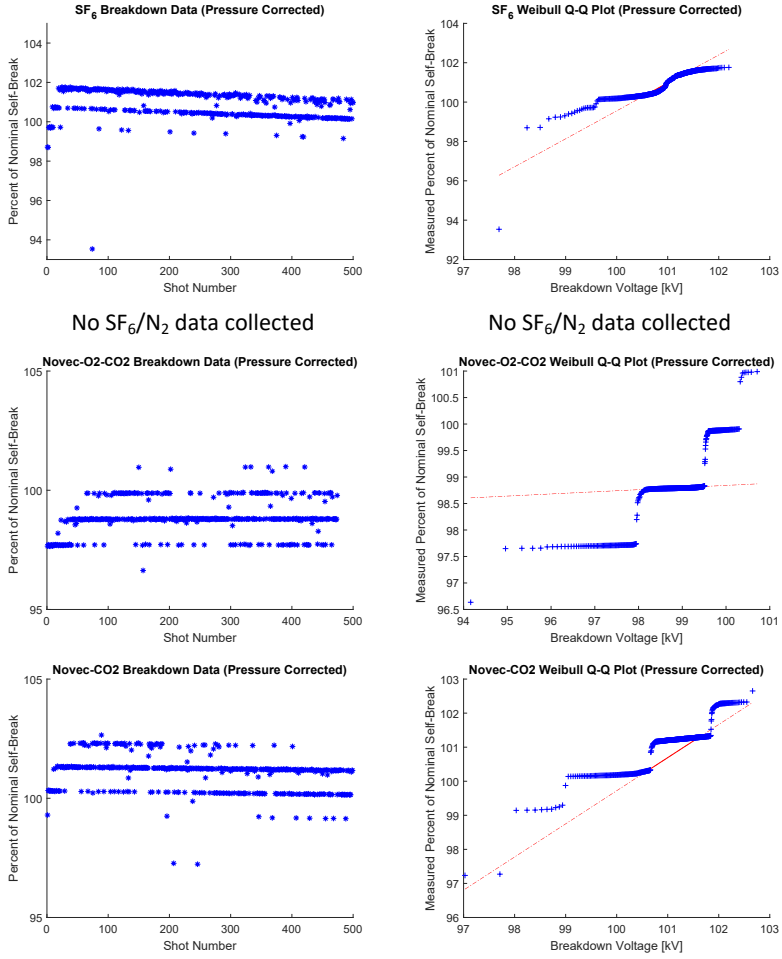

Figure 2.8. Post 5 high-energy shots for the various gases. The left column is the 500-shot sequence; the right column is that data fit to a Weibull distribution.

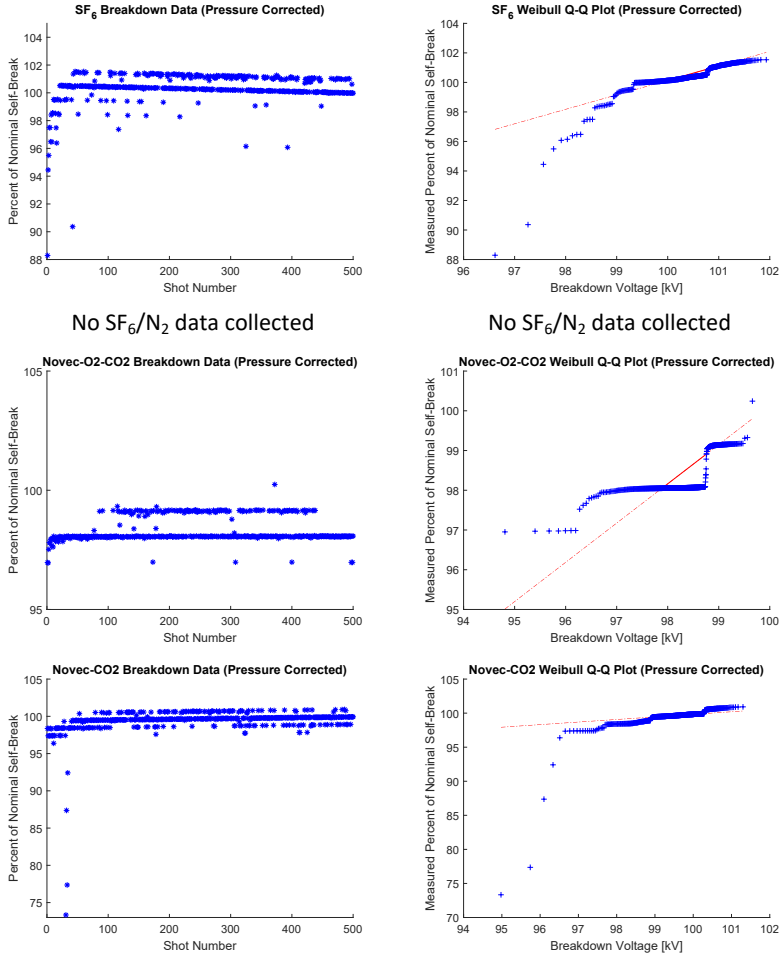

Figure 2.9. Post 10 high-energy shots for the various gases. The left column is the 500-shot sequence; the right column is that data fit to a Weibull distribution.

Table 2.1. Summary of the test sequences

Gas	Sequence	Mean Percent of Self-Break	Standard Deviation of Percent of Self-Break	Weibull Scale	Weibull Shape	Minimum Percent of Self-Break	Number of Shots Below 95th Percentile	Number of Shots Below 95% of Self Break
SF_6	Baseline	101.6	0.1267	101.6	1303	100.5	10	0
SF_6	10 J	102.2	0.6027	102.4	229.3	95.62	14	0
SF_6	30 J	101	0.7926	101.2	197	92.4	10	2
SF_6	50 J	100.9	0.705	101.2	196.1	93.54	9	1
SF_6	100 J	100.4	1.11	100.7	165.1	88.29	13	3
SF_6/N_2	Baseline	100.8	0.6587	101.2	118.4	98.11	6	0
SF_6/N_2	10 J	99.68	0.6531	100	151.1	97.3	24	0
SF_6/N_2	30 J	98.48	0.981	98.95	112.5	95.65	7	0
Novec/O_2/CO_2	Baseline	99.07	1.338	99.76	66.52	94.71	2	2
Novec/O_2/CO_2	10 J	97.92	0.5964	98.19	178.2	93.51	3	2
Novec/O_2/CO_2	30 J	99.41	1.142	100	80.84	95.43	4	0
Novec/O_2/CO_2	50 J	98.87	0.7267	99.24	130.6	96.64	1	0
Novec/O_2/CO_2	100 J	98.31	0.504	98.58	177.2	96.95	7	0
Novec/CO_2	Baseline	101.1	0.906	101.5	169.2	95.18	0	0
Novec/CO_2	10 J	101.9	0.549	102.1	206.1	100.1	6	0
Novec/CO_2	30 J	101.2	0.6484	101.5	174.2	98.15	4	0
Novec/CO_2	50 J	101.1	0.7176	101.4	156.5	97.23	11	0
Novec/CO_2	100 J	99.44	1.822	99.88	137.2	73.34	4	4

3. EXPERIMENAL GAS CHEMISTRY INVESTIGATIONS VIA RGA

In this section, the change in gas composition of the Novec insulating gas mixtures is investigated. A short literature review on similar experiments in literature is given. A discussion on the uses, complications, and limitations of the RGA for this purpose is also given. The experimental framework including vacuum chamber and residual gas analyzer (RGA), as well as data processing method, is detailed. Results are given in the final section where we investigate the introduction of trace gas species and change in species in response to high energy depositions.

3.1. Previous investigations of gas chemistry of Novec mixtures

Insulating equipment filled with Novec gas mixtures must expect the real composition of the gas to alter in response to electrical discharges. More repetitive and more energetic discharges should correlate with increasing decomposition of C4F7N and carrier gases. Note that C4F7N is principally a low GWP gas because it readily decomposes in short lifetimes, so electrically-disturbed Novec mixtures should have a rich gas chemistry.
Because C4F7N is strongly fluorinated, reactions with C4F7N and H (due to the presence of water in a real system) may ultimately produce hydrofluoric acid (HF). The mixtures Novec-O2-CO2 and Novec-CO2 may produce carbon monoxide (CO) simply due to dissociation of the CO2. C4F7N contains the cyano group CN which is generally associated with potentially toxic byproducts (for instance, HCN).
The present literature, generally, features two methods of gas composition detection applied to C4F7N: gas chromatography-mass spectrometry (GC-MS) [17, 18, 3, 19, 20, 21] and infrared spectroscopy methods including FTIR [22]. The former is particularly useful for the quantitative detection of “standard” gases (i.e. CO2, CO and common fluorocarbons). The latter is developed principally as an on-site detection mechanism not requiring laboratory-grade instruments. Note that these citations are not an exhaustive list.

3.2. Use of the RGA

The use of a residual gas analyzer (RGA) as a quantification method for C4F7N gas mixture composition has not yet appeared in literature. For this sort of work, a partial pressure (typically no more than 1e-5 Torr) of a gas of-interest may be introduced to a vacuum chamber containing an RGA typically configured to use a 70 eV electron beam. The energetic electrons will ionize neutral molecules which are accelerated and collected by a typical mass spectrometer quadrupole. An ion mass spectra (usually multiple lines due to multiple ionization pathways) is recorded with a pattern indicative of a particular neutral gas species.
RGAs have some unique benefits to this sort of work that make them an attractive option for this investigation. RGAs provide an avenue for detecting some products which are apparently not easily quantified otherwise. We will discuss HF as an example relevant to C4F7N mixtures:

- HF is likely ionized in the fashion of both: $e + HF \rightarrow 2e + HF^{+}$ and $e + HF \rightarrow 2e + H^{+} + F$, meaning a line located at 20 (and 19 via a subsequent ionization of F) is likely. This is convenient, as very few other molecules are likely to contribute to M/Q = 20. Note from [17, 18, 3, 19, 20, 21] that efforts to characterize HF content in C4F7N mixtures using a GC-MS either go uncommented or, in the case of [17], to paraphrase, fail accurate measurement and the work

relies on separate indication methods. Kieffel et al [3] comments on the presence of HF from thermal degradation but did not measure it in comparison to other by-products.

The use of an RGA in this fashion also comes with limitations and some facets which require consideration:

- The possibility of overlapping patterns interferes with the ability to distinguish the patterns of similar molecules.
- RGA's are not absolute accurate ppm measurements to any molecule in-general, though they are typically calibrated to N2. This is principally because the electron impact ionization cross-section between neutrals differs, but the effect is also contributed-to by mass and general size. It is not possible to characterize this sensitivity except for common gases sourced from leak cylinders (ex: CO2).
    - An RGA is generally "more sensitive" to SF6, for instance, than N2 because the total electron impact ionization cross-section of SF6 is much larger. The ratio between peaks indicative of SF6 is likewise based on these cross-sections.
    - Note: this is also true for vacuum ion gauges.
- Exact RGA response and sensitivity to introduced gases is, to some extent, dependent on environment (both temperature and chamber pressure) as well as chamber dimension.
    - Leak orifices generally increase leak-rate with temperature, meaning that partial pressures introduced by orifices that are "too large" for a small chamber may change significantly as laboratory temperature changes through a day. Per the previous point, this change in internal chamber pressure will disturb RGA response.
- Larger chamber pressure increases RGA measurement SNR, but excessive chamber pressure (typically exceeding 1e-5 torr) introduces space charge effects which cause RGA measurements to enter a regime of nonlinear behavior.
- Ion gauges, turbo pump oil, windows, and other common vacuum hardware are likely sources of contamination.
- RGA require significant warmup time before use, with the filament on, in order to outgas contaminants from the filament (this is a common source of CO in the chamber).
    - Introduction of gas may immediately change the "real" background of an RGA signal if this gas contains species which are prone to adhering to chamber walls (such as H2, H2O and F2)

Table 3.1. Species of interest to this work. Notes are given on how these products are detected using an RGA.

	Purpose	Indicative line (M/Q)	Notes on detection
C4F7N	Major insulating agent	69 (CF3+)	-
CO2	-	44 (CO2+)	-
O2	-	32 (O2+)	-
CO	Toxic by-product	28 (CO+)	Use ratio of 28 (CO+) to 44 (CO2+)
HF	Toxic by-product	20 (HF+)	-
C2N2	Toxic by-product	52 (C2N2+)	-
C3HF7	Bottle contaminant Zhang2019-[17]	151 (C3H56+) Zhang2019-[17]	-
HCN	Toxic by-product	27 (HCN+)	-
CF3CN	Toxic by-product	76 (CF2CN+)	Use ratio of 76 to 69 (CF3+)
C2F5CN	Toxic by-product	126 (C2F4CN+)	-
C2F6	Toxic by-product	119 (C2F5+)	-
C3F6	Toxic by-product	150 (C3F6+)	-
COF2	Toxic by-product	66 (COF2+)	-
C3F8	By-product	169 (C3F7+)	-
C2F4	By-product	100 (C2F4+)	Use ratio of 100 to 69 (CF3+)

The ion mass spectrum pattern of C_4F_7N is given by Rankovic et al [23] and reproduced in the table below, ordered from most-to-least dominant line strength.

Table 3.2. The ion mass spectrum pattern of C_4F_7N ordered from most-to-least dominant line strength.

M/Q	Relevant ion
69	CF3+
31	CF+
76	CF2CN+
50	CF2+
107	CCF3CN+
57	CFCN+
100	C2F4+ or C4F2N+
176	C4F6N+

The same is given below for CO2:

Table 3.3. The ion mass spectrum pattern of CO_2 ordered from most-to-least dominant line strength.

M/Q	Relevant ion
44	CO2+
28	CO+
16	O+
12	C+

The same is given below for O2:

Table 3.4. The ion mass spectrum pattern of O_2 ordered from most-to-least dominant line strength.

M/Q	Relevant ion
32	O2+
16	O+

Note that some by-products of interest coincide with the cracking patterns of principal gases. For example, the indicator line of CO (28) is also contributed to by CO2, and some by-products singly-ionize into ions also present in the cracking pattern of C4F7N. For these by-products, relative increases and decreases in presence is measured by normalizing to a large line of the overlapping species. In this way, an increase in H(28) may occur due to an increase in either CO or CO2, but an increase in the ratio H(28)/H(44) should occur only (or mostly) due to CO. Accurate quantitative measurements are not possible for species detected via a ratio in this way.

3.3. The experimental method

To perform a sequence of measurements, the RGA (SRS 200) is first allowed to warm-up for at least one hour in a vacuum chamber with a typical background less than 1e-7 torr. Background scans are taken of the chamber for at least 20 minutes.

Switch-a-roo is configured into the high energy configuration. Capacitors of size X nF were used. A typical single high energy shot deposits and estimated 10 J into the T-670 switch contents.

The Switch-a-roo pressurized gas system and high-pressure side of RGA addition is evacuated using a reclaimer (DILO). The RGA addition is then closed-off and allowed to remain at vacuum, typically less than 2e-1 Torr. The gas bottle is opened to fill the Switch-a-roo system to the nominal 100 kV holdoff pressure (~28 psig).

The Switch-a-roo sequence of 1,3,5, or 10 high energy shots is begun and allowed to complete. Note that this typically takes one minute per shot. The time at which this sequence ends is dubbed t_0, and this time is considered to be $t = 0$ for the purposes of RGA data processing. Once the sequence ends, the operator opens the evacuated RGA high-pressure side to the switch, which sucks the gas content into a rough vacuum region. This mixes the gas. The system pressure typically drops to 17 psig in this process.

A variable leak valve is opened to introduce this perturbed gas to the vacuum chamber and RGA, carefully opened to achieve a real pressure of 1e-5 torr as reported by a cold cathode ion gauge. The achievement of this pressure is estimated based on the gas contents according to ion gauge sensitivity. See the table below.

Table 3.5. Pressure estimated based on the gas contents according to ion gauge sensitivity

Gas Mixture	Desired cold cathode ion gauge reading	Estimated real chamber pressure
Novec-O2-CO2	1.4e-5	1e-5
Novec-CO2	1.4e-5	1e-5
SF6-N2	1.15e-5	1e-5
SF6	2.5e-5	1e-5

The RGA was then left to read scans in the gas for at least four hours from t_0. The system is monitored for pressure maintenance and adjusted accordingly. After this four hour period, the variable leak valve was closed (RGA returning to background scans), and then re-opened approximately 24 hours later to take a set of representative next-day scans. After at least 20 minutes, the variable leak valve was again closed. A final set of background scans is continued for the next 20 minutes, and then a session was complete.

3.3.1. Data processing

An as-received RGA scan is chart of Amps received per 0.1 M/Q. Many peaks center on the integer M/Q, but it is possible for the real peak to lie slightly aside, and for this exact offset to change per-peak and change with time. A histogram of this signal (with elements which are normalized to sum to 1) can be formed by bucketing this signal into elements of integer M/Q. This histogram is less brittle than the as-received scans from a data-processing perspective

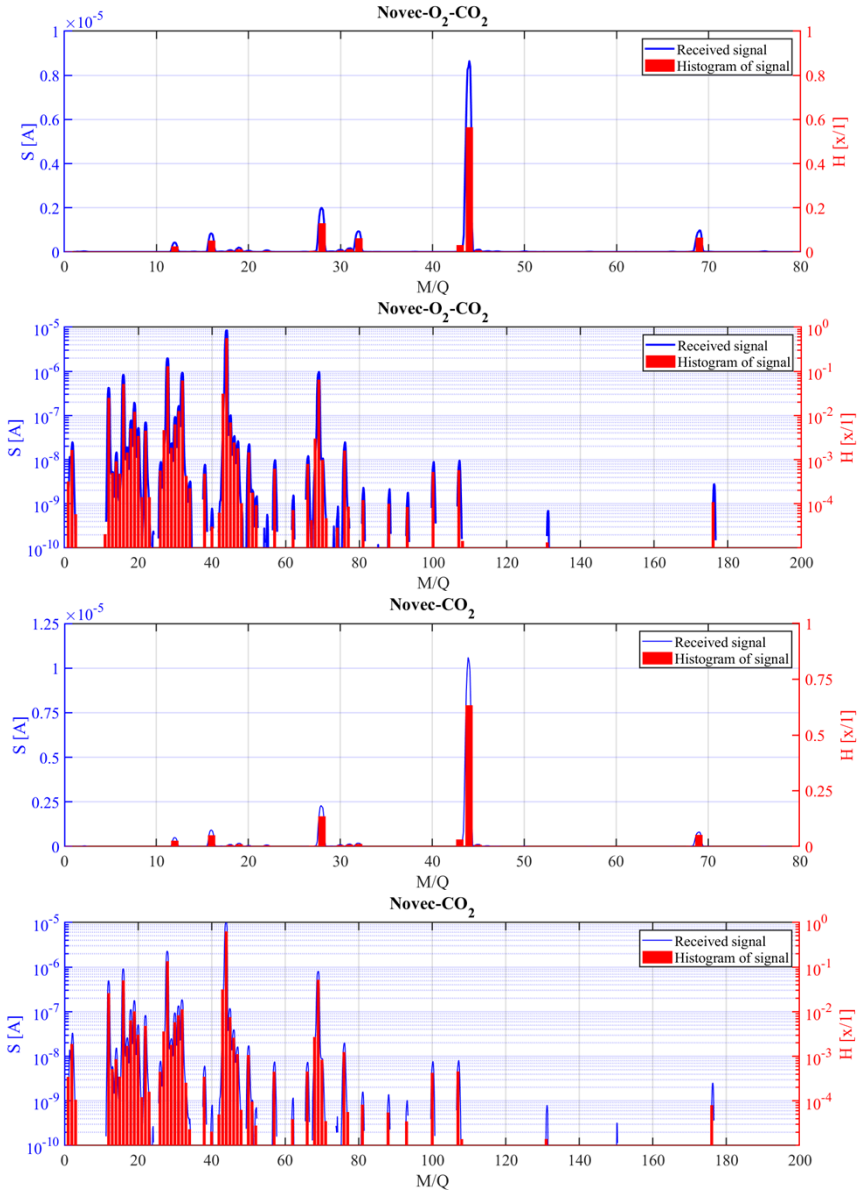

Figure 3.1. An example of the histogram procedure applied to a scan as-received. Curves are taken from the "baseline" set of scans of unperturbed gas mixtures .

Values of a histogram element are proportional to the gas content associated with the line. RGA's are not equally sensitive to all molecules, and line sums will differ by some constant factor. Based on prior observations, the observed sensitivity to constituent gases in a mixture can be estimated roughly as the following:

Table 3.6. Estimated sensitivity to constituent gases in mixture

	Novec-O2-CO2	Novec-CO2
CO2	0.5	0.5
O2	0.5	-
C4F7N	1.6	1.3

The above means that the sum of the indicative lines of CO_2 in a mixture with known CO2 content will appear smaller than expected, and that the lines of C4F7N are larger instead. Sensitivity factors can be large, but are typically within a factor of x5 for any gas.

Each RGA scan containing relevant gas measurements are pre-processed by removing a background. A set of representative background scans is selected, averaged, and then removed from all signal scans. The subsequent histogram of this signal now also lacks this background.

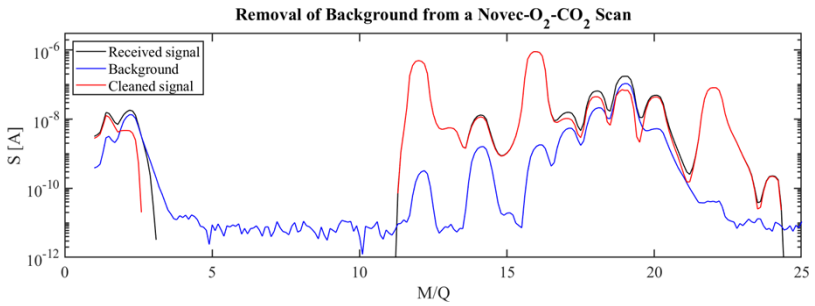

Figure 3.2. An example of the removal of a background from a scan. The largest lines reduced are typical for water (17 and 18) and Hydrogen (2)

Occasionally, fluctuations in system pressure perturb the RGA scan. Scans found to have too-large of a norm (sum of area beneath the curve) compared to more-typical scans are removed and treated as outliers. The "typical" error is treated as the coefficient of variation:

$$\epsilon = std(x)/mean(x)$$

All errors here are given in percent. A error of +- 1.2% in received scan norm was typical in this way.

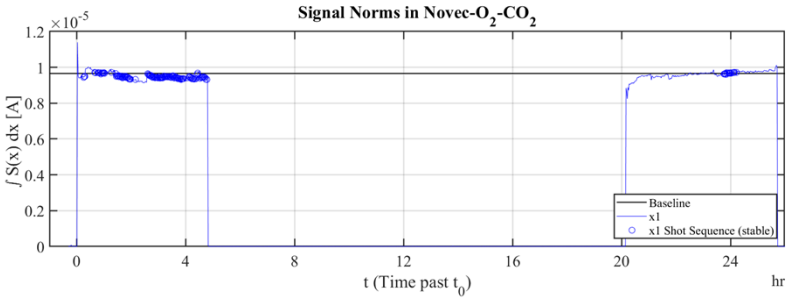

Figure 3.3. An example of the norms of all received scans. The typical norm for the baseline scan sequence is given in black. Scans which were kept for plotting and further processing are selected with circles. Past 20 hours, scans were only selected if they were also taken within +- 30 minutes of the point in time 24 hours post t0. Signal norm is nearly zero before t = 0 and between t = 5 and t = 20 because this is the period the leak valve was closed.

An example of the norms of all received scans. The typical norm for the baseline scan sequence is given in black. Scans which were kept for plotting and further processing are selected with circles. Past 20 hours, scans were only selected if they were also taken within +- 30 minutes of the point in time 24 hours post t0. Signal norm is nearly zero before t = 0 and between t = 5 and t = 20 because this is the period the leak valve was closed.

In the following section, where results are reported, the indicative lines (or ratios between lines) which indicate relevant species are taken from histograms for scans up to 4 hours past t0 per shot sequence. For clarity, data points are grouped per 15 minutes. Data are selected only from scans deemed “valid” because their scans posses acceptable norms. Thus, data appear missing in the case where RGA behavior was not stable enough to capture a reliable scan.

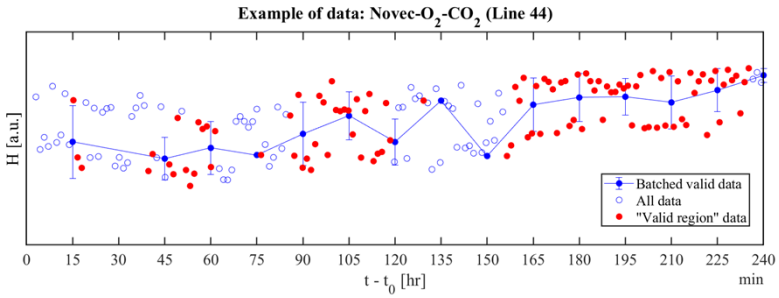

Figure 3.4. Example of RGA data for Novec-O2-CO2 mixture. Indicative lines (or ratios between lines) which indicate relevant species are taken from histograms for scans up to 4 hours past t0 per shot sequence. Data points are grouped in 15 minute intervals.

The typical variance of a value recorded at a single M/Q increases as the real signal strength decreases. This means that lines associated with trace by-products have a significantly larger experimental error than the lines associated with major gases. This error per-line, found in the same fashion as the overall error of the scan, is also given on the plots (in gray patches). Changes from the baseline capture within the gray patch, then, are within experimental error. Note that real experimental error, given by the gray patch, is treated assuming the overall scan error and line error are additive, meaning:

$$\epsilon = \sqrt{\epsilon_{scan}^2 + \epsilon_{line}^2}$$

Experimental errors known per-line per gas-mixture are given below. Note that typical error ϵ_{scan} is within +-3%.

Table 3.7. Experimental errors known per-line per gas-mixture

	Indicative line (M/Q)	Line error (Novec-O2-CO2)	Line error (Novec-CO2)
C4F7N	69 (CF3+)	0.71%	0.72%
CO2	44 (CO2+)	0.27%	0.51%
O2	32 (O2+)	0.28%	0.47%
CO	28 (CO+)	0.24%	0.35%
HF	20 (HF+)	0.65%	1.42%
C2N2	52 (C2N2+)	10.68%	17.30%
C3HF7	151 (C3H56+)	Not observed in baseline	Not observed in baseline
HCN	27 (HCN+)	2.77%	11.07%
CF3CN	76 (CF2CN+)	1.19%	1.12%
C2F5CN	126 (C2F4CN+)	136.29%	251.46%
C2F6	119 (C2F5+)	77.92%	110.76%
C3F6	150 (C3F6+)	62.46%	115.83%
COF2	66 (COF2+)	3.70%	1.47%
C3F8	169 (C3F7+)	Not observed in baseline	Not observed in baseline
C2F4	100 (C2F4+)	1.74%	3.00%

3.4. Experimental results

3.4.1. Results For Novec-O2-CO2

Table 3.8 summarizes the analysis for presence of gas constituent trends for Novec-O2-CO2 at baseline, and after 1, 3, -5, and 10 shots. The data supporting this table is shown in Appendix A.

Table 3.8. Species of interest for Novec-O2-CO2 with notes are on how these products are detected.

	Purpose	Indicative line (M/Q)	Estimate presence	Response to shots
C4F7N	Major insulating agent	69 (CF3+)	5e-2	Inconclusive
CO2	-	44 (CO2+)	6 e-1	Inconclusive
CO	Toxic by-product	28 (CO+) (28/44)	-	Increases with shots
HF	Toxic by-product	20 (HF+)	2 – 4 e-3	Increases near t0
C2N2	Toxic by-product	52 (C2N2+)	2 – 10e-5	Increases with shots
C3HF7	Bottle contaminant Zhang2019-[17]	151 (C3HF6+) Zhang2019-[17]	Never observed	-
HCN	Toxic by-product	27 (HCN+)	2 – 6 e-3	Increases near t0, and with shots
CF3CN	Toxic by-product	76 (CF2CN+) (76/69)	-	No significant change
C2F5CN	Toxic by-product	126 (C2F4CN+)	0 – 8 e-6	No significant change
C2F6	Toxic by-product	119 (C2F5+)	0 – 2e-6	Significant increase
C3F6	Toxic by-product	150 (C3F6+)	0 - 2e-6	No significant increase
COF2	Toxic by-product	66 (COF2+)	6 – 10e-4	Increases over time
C3F8	By-product	169 (C3F7+)	Never observed	
C2F4	By-product	100 (C2F4+) (100/69)	-	Slight increase near t0

3.4.2. Results for Novec-CO2

Table 3.9 summarizes the analysis for presence of gas constituent trends for Novec-CO2 at baseline, and after 1, 3, -5, and 10 shots. The data supporting this table is shown in Appendix A.

Table 3.9. Species of interest for Novec-CO2 with notes are on how these products are detected.

	Purpose	Indicative line (M/Q)	Estimate presence	Response to shots
C4F7N	Major insulating agent	69 (CF3+)	-	Inconclusive
CO2	-	44 (CO2+)	-	No significant change
CO	Toxic by-product	28 (CO+) (28/44)	-	No significant change
HF	Toxic by-product	20 (HF+)	2 – 3 e-3	Increases with time
C2N2	Toxic by-product	52 (C2N2+)	2 – 13 e-5	Significant increase
C3HF7	Bottle contaminant Zhang2019-[17]	151 (C3HF6+) Zhang2019-[17]	Never observed	-
HCN	Toxic by-product	27 (HCN+)	2 – 7 e-3	Increases
CF3CN	Toxic by-product	76 (CF2CN+) (76/69)	-	No significant change
C2F5CN	Toxic by-product	126 (C2F4CN+)	0 – 1 e-5	Significant increase
C2F6	Toxic by-product	119 (C2F5+)	0 – 2 e-5	Increase over 24 hr
C3F6	Toxic by-product	150 (C3F6+)	0 – 3 e-5	Increase near t0
COF2	Toxic by-product	66 (COF2+)	5 – 10 e- 4	Increases over time
C3F8	By-product	169 (C3F7+)	Never observed	-
C2F4	By-product	100 (C2F4+) (100/69)	-	Slight increase

3.5. Conclusions

This experiment intends to investigate two specific qualities in response to high energy depositions:

1. To quantify the extent of C4F7N dissociation (reduction in C4F7N content)
2. To detect the presence or absence of certain trace by-products

3.5.1. Magnitude of C4F7N and CO2 dissociation

The available data from these measurements is not significant to address #1. This is principally because the attempted quantification of change in Novec proportion compared to baseline scans provide inconsistent and often unrealistic answers, implying experimental uncertainty larger than the

measurement. Most tests in both Novec-CO2-O2 and Novec-CO2 imply decreases in Novec content on the order of 15%. In the case of Novec-CO2, the 5 shot sequence suggests a major *increase* in content instead.

Note that Kieffel et al [3] evaluated the change in concentration of C4F7N in arced Novec-CO2 to be small (~ 1% from the nominal 4% presence in mixture). From Zhang et al [17] paraphrasing Radisavljevic et al, the dissociation energy of Novec can be estimated as 0.24 mol/MJ. The maximum energy deposition in a test for this work is 100 J (ten shots). These values suggest the measured changes in Novec concentration would be expected on the order of *ten thousand* high-energy shots. Additionally, the manner of change (increasing/decreasing in response to increasing shot number) is inconsistent.

We expect that the data's suggestion of mass dissociation of Novec does not reflect the real gas composition of switch contents. Such dissociation would certainly decrease breakdown voltage, or at least worsen breakdown statistics. On the contrary, no significant impact on breakdown behavior was observed in any breakdown-distribution tests. It is worth note that, as is pointed out by Zhang et al [17], fluorocarbon products which C4F7N is likely to dissociate-into are *also* strong insulators, so the reduction in breakdown potential due to dissociation may be mitigated in real systems.

In light of the large uncertainty implied by the Novec concentration results, the measured changes in CO2 (expected to decrease as CO concentration increases) do not well-exceed experimental error of the system and cannot be addressed conclusively.

It is possible the difficulties in addressing #1 are due to an inability to capture a representative baseline scan in a gas mixture which is valid for comparing long-time-scale scans. This may explain data like that of (69) where the number of shots does not correlate with a behavior trend. It is not known if taking new baseline scans per-day just-before conducting tests are an effective way to address this issue.

3.5.2. Presence/absence of certain products

The work can, however, successfully address #2. Of all compounds listed in Table 3.9, all but the non-toxic by-product C3F8 and common contaminant C3HF7 were observed. Of note, these products were observed in *both* unperturbed gas as well as perturbed samples. This means that a bottle of received Novec mixture contains some trace by-products at very small quantities, rather than being "clean", and that most of these products are of similar orders of magnitude to those found post-discharge.

An increase in CO content is observed in Novec-O2-CO2 mixtures, but not significantly observed in Novec-CO2. The detection of products HF, C2N2, HCN, C2F5CN, C2F6, C3F6, and COF2 is certain due to presence at unique line locations. It is of note that previously-cited GC-MS work has observed these products in post-discharge conditions, but from [17], apparently cannot distinguish the small quantities we found to be present in the unperturbed gas. Increases in line strengths indicative of CO and C2F4 are less certain due to strong uncertainty in the ability to measure the comparison line.

The by-products with the most significant presence observed were HF, COF2, and HCN. While these line strengths are certainly not equivalent to the real ppm in the gas, they can be expected to be accurate in order of magnitude. Thus these three products may be present on the order of 1000 ppm (line strength H ~= 1e-3) each. Based on the curvature of data, quantity of HF and HCN tends to decrease with time while COF2 increases and remains in larger quantity over 24 hours.

The quantities of product C2F5CN, C2F6, and C3F7 was found to be larger (~x10) in the Novec-CO2 mixture than the Novec-O2-CO2 mixture. Some strong increases in C2F6 content were observed in the Novec-O2-CO2 mixture, and somewhat less-so in the Novec-CO2 mixture. In the former, relative increases of up to x1000 were observed.

We stress that the RGA data support the presence or absence of byproducts of interest, but that quantitative data on concentration should be viewed as preliminary at best, considering the large experimental uncertainties uncovered in measurements of the parent Novec molecule. Further tests including GC-MS are warranted for more sensitive measurements of persistent byproducts.

3.5.3. Final notes

RGA measurements indicate that Novec gas mixtures may contain toxic components, some of which are present in the unperturbed gas, and concentrations may increase after discharges between 10 and 1000 joules/liter. Some of these byproducts remain in the mixture over long time periods (~24 hours). Of these, HF, HCN and COF2 may have concentrations high enough to pose acute inhalation hazards; however, the relative volume of arced gas released into the breathing space of members of the workforce would have to be so large that the Novec mixture would take up at least order percent of the breathable atmosphere. Byproducts present at the scale of small (few liters or lower) spark gaps are very unlikely to pose a significant hazard to personnel; however, tests at larger scales are warranted to determine if the hazard grows with larger switches, such as the laser triggered gas switches on Z, Saturn, and other large accelerators.

The RGA method cannot reliably detect percent dissociation of C4F7N and cannot be used to conclude the influence of this dissociation on changes/lack-of-changes in breakdown behavior. Indicative lines of the expected product C3F8 and expected bottle contaminant C3HF7 were never observed in any test.

It may be worthwhile to repeat tests in C4F7N with an experimental framework that can reliably measure absolute ppm in HF, HCN, COF2 and CO for which an RGA is not well-suited. Note that from previously cited literature that a GC-MS may not be capable of accounting for all products of importance, and separate indication methods may be required for some of the more interesting by-products.

4. PLASMA CHEMISTRY MODELLING OF NOVEC 4710

4.1. Overview

A zero-dimensional plasma global model is used to simulate the plasma arc decay and recombination process in spark-gap switches relevant to the Z machine. The basic capability was originally made at Sandia to study laser-driven ionization mechanisms in a Single Particle Aerosol Mass Spectrometer [25]. The purpose of this work is to determine the composition of the post-arc gas after a switching process in which the arc-quenching medium is a mixture of Novec 4710 (C_4F_7N) and CO_2. Special attention is given to long-lived species that are considered toxic. In this summary, we report the basic description of the global model and the modifications and assumptions used to configure this model to simulate the switching process. The available reaction data with regards to Novec 4710 and CO_2 is gathered to build a reaction set capable of modelling the arc and decay. Benchmarking and conservation checks are used to strengthen confidence in the model's capabilities. Preliminary results with a CO_2 arc show the presence of long-lived species after a single switching process.

4.2. Arc Model description

The global model uses Python's "scipy.integrate.odeint" function to solve a set of differential equations. This function uses an algorithm called LSODA, which automatically detects the stiffness of the system and can switch between the nonstiff Adams method and stiff backward differentiation formula methods. The general governing equation for the species densities is described as,

$$\frac{dn_s}{dt} = \sum_j^{rxns}\left(a_{s,j}^{RHS} - a_{s,j}^{LHS}\right)R_j,$$

Where n_s is the density of species, s, the stochiometric coefficient of reaction, j, is defined as a, and RHS and LHS refer to the right hand side and left hand side of the reaction, respectively. The reaction rate is $R_j = k_j\prod_s^{LHS} n_s$, where k_j is the rate constant of the reaction. The two remaining governing equations are for the electron energy and heavy species (ions and neutrals) energy, which required some modification for application to the arc decay process. After reviewing literature on spark gap switches and plasma arc modelling (Zhong, Wang, Xu, Wang, & Rong, 2019; Gnybida, Rümpler, & Narayanan, 2019; Lowke, 1979; Kushner, Milroy, & Kimura, 1985; Bindu, et al., 2012), it was decided to simulate an arcing process through power deposition to the electrons, assume that the electrons always follow a Maxwellian distribution, and include radiation as a power loss mechanism for the heavy gas species. Thus, the governing energy equations are,

$$\frac{\partial(\frac{3}{2}k_b n_e T_e)}{\partial t} = \frac{P_{dep}}{Vol} + \sum_j^{rxns}\Delta\epsilon_{e,j}R_j, \text{ and}$$

$$\frac{\partial(\frac{3}{2}k_b n_g T_g)}{\partial t} = -\epsilon_R\sigma T_g^4\left(\frac{SA}{Vol}\right) + \sum_j^{rxns}\Delta\epsilon_{g,j}R_j$$

where P_{dep} is the power deposition, $\Delta\epsilon$ is the energy exchange due a reaction, ϵ_R is the emissivity of the heavy species, σ is the Stefan-Boltzmann constant, SA is the surface area of the arc, Vol is the volume of the arc, and e and g refers to the electrons and heavy gas species, respectively. The energy exchanges from reactions are determined using the change in enthalpy

of formation of the reaction and additional information from the reaction data source. Note, that volumetric expansion and diffusion terms are not included, leaving their effect for future work.

4.3. Reactions

The C_4F_7N/CO_2 reaction set involves 191 reactions including 37 decomposition/dissociation, 31 ionization/attachment, 36 recombination, 25 charge exchange, 31 neutral reactions, 25 elastic reactions, and 6 vibrational reactions. The 56 different species involved in this model are: e^-, C_4F_7N, CO_2, C_2F_3N, C_2F_4b, CF_3, N_2, CF_4, CF_2, CF, C, F, CO, O_2, O, F_2, N, C_3F_4Na, NO, CN, CF_2O, CFO, CNO, N_2O, CF_3^+, CF_2^+, CF^+, CO_2^+, CO^+, $C_2F_4b^+$, F^+, F_2^+, O_2^+, N_2^+, C^+, O^+, N^+, F^-, NO^+, CN^+, C_2F_5, C_3F_7a, C_4F_6Na, C_2FNa, C_2F_4a, C_3F_3Na, C_3F_6a, C_3F_7b, C_3F_4Nb, C_3F_4Nc, C_3F_4Nd, C_3F_4Ne, C_3F_6b, C_3F_6c, C_3F_6d, C_3F_3Nb. Note the lowercase letters at the end of the species name denotes the particular molecular structure of that species. The decomposition reactions are critical for breaking down Novec 4710 into smaller components that have more available data for plasma chemistry and reaction with CO_2. However, just as important, is the recombination of the Novec 4710 products after the arc has passed. Thus, all the decomposition reactions are accompanied with their corresponding reverse reaction. Calculation of the reverse reaction rate uses the forward rate constant and the change in entropy and enthalpy of formation of the reaction (Chen, Zhang, Xiong, Li, & Murphy, 2019). Note that the enthalpy and entropy values are temperature dependent, with expressions available up to 5000 K. Based on decomposition tests and for simplicity, we use the enthalpy and entropy values at 300 K for these reactions for all temperatures.

Dissociation, ionization, and dissociative ionization reactions are important for the early arc phase, for they are an important transfer of energy from electrons to the heavy species and formation of ions. Certain dissociation and ionization reactions involve additional loss of electron energy (beyond the change in enthalpy of the reaction) due to an intermediate metastable state, which results in additional energy gain for the heavy species (Itikawa, 2015; Tarnovsky, Kurunczi, Rogozhnikov, & Becker, 1993). Charge exchange and recombination also play an important role in increasing the heavy species temperature and returning to a neutral dominant composition near the end of the arc decay. We implemented a generalized ion-anion neutralization rate due to the significant presence of the F^- anion (Hickman, 1979). Three body recombination is also included, considering reactions where electrons or all the heavy species (denoted as "M") act as the third body. It is important to note that any recombination reaction in which an electron is removed receives an additional loss of $\frac{3}{2}k_bT_e$ for the electron energy, which is given to the heavy species energy. This is done to avoid any artificial increase to the electron temperature.

The elastic collisions are crucial for the transfer of electron energy and heavy species energy, where power deposition is a major input to the electrons and radiation is the major output for the heavy species. Elastic collision rates are included for most major neutral species, and Coulomb collisions are included for all ion species. Lastly, vibrational reactions are also included with Novec and CO_2 to aid in the initial transfer of electron energy to heavy species. Early tests showed that the few plasma reactions with Novec are insufficient to transfer the

power deposition from electrons to heavy species at a fast enough rate, resulting in the electron temperature to increase to unreasonable levels. For simplicity, the vibrational reactions are included purely as an energy exchange mechanism; no vibrational states are directly modelled, for we assume an immediate vibrational-translational relaxation.

4.4. Benchmarking

A simple heat bath test is used to benchmark the global model with the source of Novec 4710 decomposition rate constants (Chen, Zhang, Xiong, Li, & Murphy, 2019). In this test, the heavy species temperature is fixed to 1500 K, and there are no updates to the electron and heavy species energy equation. The initial condition is pure Novec 4710 at a density of $4.83 \times 10^{24}\ m^{-3}$ (corresponding to 10^5 Pa) and the enthalpy and entropy of formation of the species are evaluated at 1500 K. Figure 4.1 shows the resulting decomposition of Novec 4710 at these conditions. The majority of the decomposition occurs over 100 seconds and results with C_2F_3N and C_2F_4b as the top products. The products with mole fraction larger than 0.01 agree with the reference's results (Chen, Zhang, Xiong, Li, & Murphy, 2019), although there are discrepancies with the products with mole fraction smaller than 0.01.

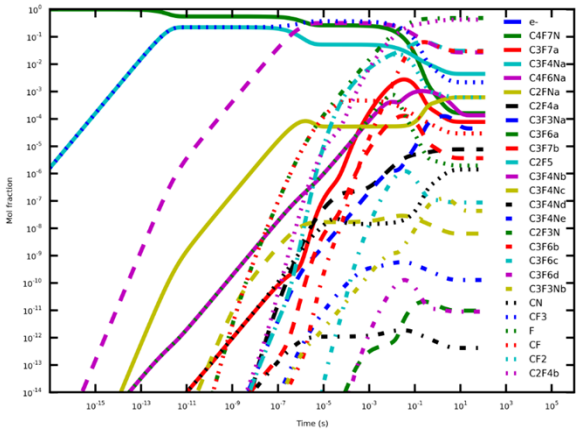

Figure 4.1. Novec 4710 heat bath test at 1500 K and 10^5 Pa

In addition to this benchmarking, the model includes mass, charge, and energy conservation checks. Subsequent arc decay simulations maintain that the maximum difference in mass and charge density is less than 10^{-5} percent. The maximum difference in total energy is less than one percent.

4.5. Arc Decay Results

For the arc decay simulation, the power deposition is described as sinusoidal ramp up, plateau region, and sinusoidal ramp down. The total time of power deposition is approximately

136 ns with a power of 10^8 W at the plateau region such that the total deposited power is 10 J. The relevant simulation parameters are summarized in Table 1.

Parameter	Value
Total Power deposition	10 J
Initial electron density	10^{23} m^{-3}
Initial Pressure	2×10^5 Pa
Arc radius	1 mm
Arc length	5 mm
Emissivity	1

Our model initializes with the assumption that the arc is already established, which allows for a simpler initial condition. We can thus initialize with a considerable electron density and maintain a fixed arc radius. The fixed arc radius and initial electron density is chosen based on review of other arc modelling work (Wang, et al., 2016; Kushner, Milroy, & Kimura, 1985). Figure 2 shows the resulting mole fractions, temperatures, reaction rates, and energy components for an arc decay simulation using pure CO2.

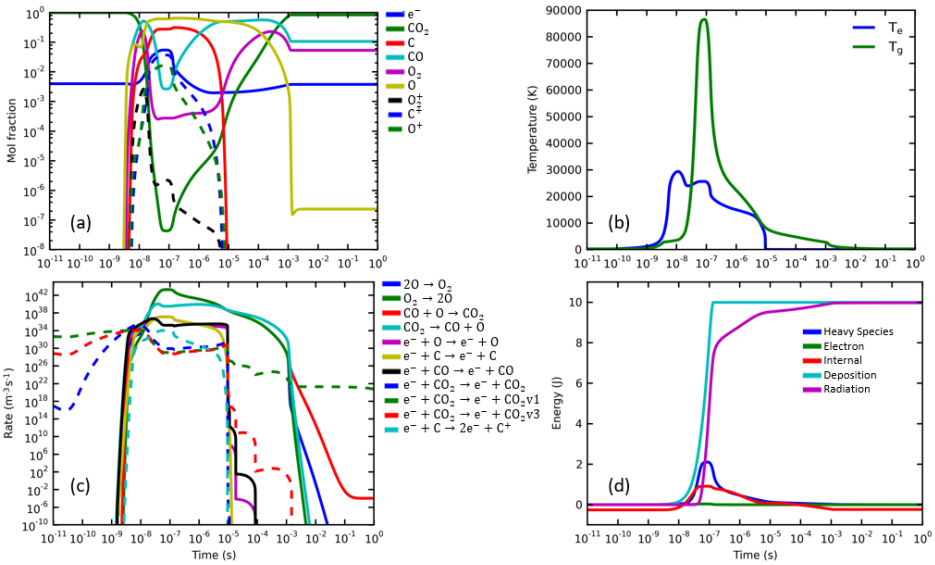

Figure 4.2. (a) Mol fraction of major species, (b) electron and heavy species temperature, (c) largest reaction rates, and (d) energy components from the arc decay simulation

The results show the growth and decay of the arc through the rise and fall of ion and electron densities and temperatures. After the arc passes, the gas composition reaches an equilibrium at around 0.1 seconds. The post arc gas composition is mainly CO_2, with CO as the next dominant species at a mole fraction of around 0.1. Given that CO is a toxic molecule, this result suggests that any switching process with a dominant CO_2 composition could lead to a build up of CO. Figure 4.2(c) shows the largest reaction rates, where decomposition and elastic reactions

dominant during the arc phase, and vibrational reactions remain relevant throughout the simulation. Figure 4.2(d) tracks the energy components that contribute to the total energy of the system, where the heavy species and electron energies are $\frac{3}{2}k_b n_g T_g$ and $\frac{3}{2}k_b n_e T_e$, respectively. The "Internal" component is defined as the weighted sum of the enthalpy of formation of the heavy species. It can be seen during the arc phase that the heavy species and internal energy become significant, and most of the 10 J deposited into the arc is removed by radiation loss. This model can be improved upon with a CO_2 arc benchmark as well as including more species and reactions. In particular, it may be beneficial to model the vibrational species rather than assume immediate VT relaxation, for it could prevent the unexpectedly large temperature increase of the heavy species that is seen in Figure 4.2(b).

5. GENERATION AND OPTIMIZATION OF CROSS-SECTIONS FOR ELECTRON-C_4F_7N COLLISIONS

A complete and consistent set of electron-neutral collision cross-sections for the novel insulating gas C_4F_7N is reported. The set is composed of a combination of cross-sections previously reported in literature, optimized via a genetic algorithm in conjunction with a multi-term Boltzmann equation solver, and calculated *ab initio* using the R-matrix code Quantemol-EC. The finalized set accurately reproduces reported macroscopic rate and transport coefficients as well as Townsend coefficients and critical electric field strengths in C_4F_7N and its mixtures with nitrogen, carbon dioxide, and argon.

5.1. Introduction

Increased attention has recently been paid to the replacement of the potent greenhouse gas SF_6 in gas-insulated spark gaps, switchgears, arc interrupters, and other high voltage systems [36-39]. The fluorinated nitrile C_4F_7N (i.e. 3M Novec 4710 Insulating Gas [40, 41]), a novel insulating gas, is one of the more interesting candidates for this purpose. Pure C_4F_7N can achieve more than twice the DC breakdown strength of pure SF_6 while possessing only one-tenth the global warming potential (GWP). A typical industrial C_4F_7N mixture, such as g3 ("green gas for grid"), meets as little as 1% the GWP of SF_6 [42].

Owing to this interest, C_4F_7N has received much attention in research. Studies reporting its chemical decomposition pathways [43–45], transport [46], thermal plasma properties [47,48], electrical breakdown [49,50], toxicity [51], and materials compatibility [52] have been reported. Several works have also reported the IR [53–55] and UV [56,57] spectra in C_4F_7N. Electron swarm parameters (transport, growth, and rate coefficients) have been measured in pure C_4F_7N and its mixtures by pulsed Townsend experiments [58–61] as well as steady-state Townsend experiments [62–65]. Models of the electrically insulating behavior of C_4F_7N are limited, however, while its collision cross-sections remain mostly unknown.

There is a need for a set of electron-neutral collision cross-sections for C_4F_7N which is both "complete" (i.e. inclusive of elastic momentum transfer, vibrational excitation, electronic excitation, ionization, and attachment collisions for a wide range of the incident electron kinetic energy ε) and "consistent" (i.e. capable of reproducing experimentally measured electron swarm parameters in a kinetic model [66]). Low temperature plasma (LTP) models rely on sets of cross-sections for the kinetic description of plasma to supply transport coefficients for fluid models [67] and reaction rates for zero-dimensional plasma global models. For many species, sets of cross-sections can be collected from literature (e.g. [68]) or compiled in a database such as the LXCat project [66,69,70]. Only very recently has one set of C_4F_7N cross-sections been reported [61]. The absence of descriptive complete and consistent sets of cross-sections for C_4F_7N, and other interesting novel gases, in general, poses a barrier to the wide-spread adoption of C_4F_7N for many applications, including pulsed power.

To develop a cross-section set, a variety of techniques may be utilized. Cross-sections may be measured experimentally in limited regimes of electron energies by electron beam or ion collection experiments such as has been done for C_4F_7N [71]. Cross-sections for some collisions can be estimated via quantum mechanical models (such as the Born approximation [72,73]) or calculated using computational chemistry methods (such as R-matrix [74,75] or complex potential [76,77] methods). Both methods have limitations; collisional beam experiments can be expensive, and *ab initio* calculation techniques can be of limited accuracy for heavier and more-complex molecules.

In the face of these obstacles, developing a cross-section set via the iterative "swarm" optimization procedure has become common, where a set of initial cross-sections are manually adjusted and assessed via an LTP kinetic model until the desired consistency is achieved. Experimental datasets of electron swarm parameters, such as the density-reduced effective ionization rate coefficient $k_{eff}/N = k_{iz}/N - k_{att}/N$ (where k_{iz} and k_{att} are the ionization and attachment rate coefficients, respectively), bulk drift velocity W (or bulk electron mobility $\mu = W/E$), and density-product bulk longitudinal diffusion coefficient $D_L N$ for a wide range of density-reduced field strengths E/N in units Td= 10^{-21} Vm^2 (where N is the gas particle density in units m^{-3}) are essential for this procedure. Examples of recent works which develop cross-section sets in this manner can be found for CO_2 [78], CO [79], H_2O [80], and the previously mentioned recent set in C_4F_7N [81].

The manual swarm optimization procedure has a steep learning curve. Efforts that attempt to abstract at least part of the manual procedure have been explored. Of note are optimization algorithms of several kinds [81,82], particularly machine learning and neural networks [83, 84]. One method in the subject of machine learning, the population-searching genetic algorithm (GA) method (for reference, see [85]) has not yet been applied for this task in literature. GA methods are well-suited to finding acceptable solutions in a large parameter space with frequent local error minimums.

Since both manual and programmatic optimization methods require thousands of swarm parameter calculations, the LTP kinetic model in use becomes the primary computational bottleneck. Options for the kinetic model include stochastic Monte Carlo Collision (MCC) models (e.g. MAGBOLTZ [86], METHES [87], and LoKI-MC [88]) and deterministic Boltzmann equation (BE) models (e.g. the "two-term approximation" models BOLSIG+ [89] and LoKI-B [90]). This study employs the publicly available multi-term BE (MTBE) code MultiBolt [91–93]. MultiBolt (currently version v3.1.0) has recently seen development that allows modeling the effects of gas temperature, superelastic collisions, and anisotropic electron scattering.

The use of an MTBE model for this purpose is of note. Kinetic model calculations for gases with large inelastic cross-sections or high E/N conditions may be poorly served by two-term BE solvers [94,95]. The task of optimizing a cross-section set for C_4F_7N is likely to be affected in this way since insulating gases tend to have large inelastic cross-sections, and the parameters of pure C_4F_7N are only experimentally known for $E/N > 700$ Td [91, 93]. Thus, a sizeable term-based error may be folded into the cross-section set without using an MTBE. While this error can also be avoided by using an MCC model, the MTBE method is selected for this work to take advantage of fast calculation speeds. MCC models may be slow to converge in strongly ionizing and attaching gases.

The goal of this work is to generate and optimize a complete and consistent set of electron-neutral collision cross-sections for C_4F_7N. In the pursuit of this, a complete set has been developed by a GA method unique to this work and complemented by *ab initio* calculations via the commercial R-matrix software Quantemol Electron Collisions (QEC) [108]. This report is structured as follows. Section 2 discusses the GA and R-matrix methods. Section 3 reports the results of these methods and the finalized set formed from the composite between the two. Swarm parameter calculations are given to evaluate the cross-section set. Finally, in section 4, remarks on the techniques applied, their limitations, and subjects of future investigation are given.

5.2. Background

The final set of cross-sections reported in this manuscript is a combination of those available in the open literature, those inferred from swarm data using a GA and MTBE code, and those calculated using QEC. This section will detail each of these models and existing data.

5.2.1. Genetic algorithm

In this section, the generation of a complete parameterized cross-section set via a population-searching GA method is discussed.
A GA searches a space of parameters for a solution to a particular problem by "evolving", in a manner resembling survival-of-the-fittest, a population of poor solutions towards better solutions [94]. For each generation of evolution, a pool of individuals whose traits are defined by a "genome" $\mathbf{x} = \{x^{(1)},x^{(2)},...x^{(m)}\}$, a sequence of m

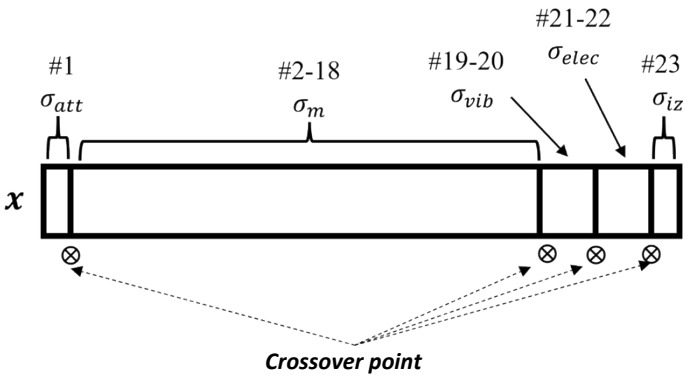

Figure 5.1. Construction of the cross-section genome. Each section of the genome, a locus, is associated with the creation of a different kind of cross-section. The labels σ_{att}, σ_m, σ_{vib}, σ_{elec}, σ_{iz} denote sections dedicated to drawing the attachment, elastic momentum transfer, vibrational excitation, electronic excitation, and ionization cross-sections respectively. *Figure source*: [105].

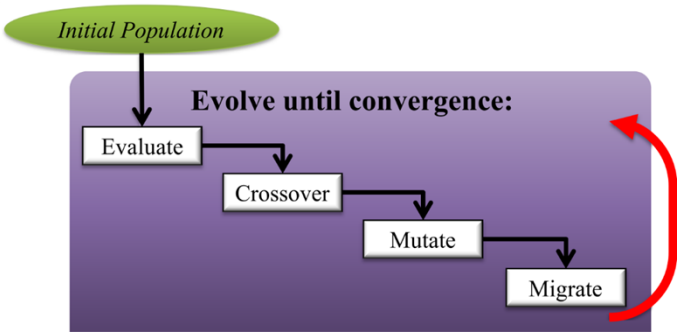

Figure 5.2. Flowchart of the GA procedure. The "migrate" procedure occurs once every fifth generation, while other procedures occur once per-generation. *Figure source*: [105].

"chromosomes", are each assessed for their ability to solve a certain problem via a "fitness function". The most-fit individuals (i.e. those that most closely replicate the desired results), "parents", are chosen to undergo "crossover" to create the next generation's population. Variety is introduced by mutation, wherein a small random proportion of all chromosomes in all offspring change value. The average fitness of the whole population rises as generations progress and better solutions are found. The process repeats until an acceptable answer has been found or the population has stopped improving between generations.

For the GA used to conduct this study, each $x^{(1,2,\ldots m)}$ were parameters of the cross-section set. The genome of each individual, depicted in Figure 5.1, was constructed as an array of numbers in the range [0,1] and split by sections of chromosomes relevant to the construction of each kind of cross-section. These individuals were interpreted into candidate cross-section sets and

then input to the MTBE model. The calculated electron swarm parameters were compared against fits to the experimental pulsed Townsend swarm data of Chachereau *et al.* [67] for the mixtures of 94.85%-5.15% N_2-C_4F_7N, 59.67%-40.33% CO_2-C_4F_7N, and 100% C_4F_7N. Cross-section sets that reproduce the bulk drift velocity W with the smallest mean absolute error were chosen to be parents and propagate their traits between generations.
To avoid early convergence and improve solution variety, some techniques were applied in this work.

- Mutation: post-crossover, a random number of individual chromosomes are replaced with new values. The mutation rate for all chromosomes was fixed at 5% for random replacement and 20% for a random $\Delta \in \pm 5\%$ perturbation of the chromosome value.
- Islanding: the total population pool is split into smaller isolated pools (”islands”). In this work, a GA instance uses 128 total individuals split into eight islands given 32 individuals each.
- Migration: chosen individuals occasionally participate in crossover in a different island than where they started. Migration occurs every 5th generation.
- Elitism: best-fit population members, called “elites”, remain in the population for crossover between generations. Per generation, two unique elites are selected to remain in the crossover pool per-island.

A four-point locusing crossover procedure was applied to generate offspring for new generations. Each section of the genome dedicated to the construction of a different kind of cross-section is one locus. Crossover points are fixed on the dividing lines between loci. To perform crossover, an offspring $\mathbf{x}_C$ is created by linear interpolation between two parents $\mathbf{x}_A$ and $\mathbf{x}_B$.

$$\mathbf{x}_C = \lambda \mathbf{x}_A + (1 - \lambda)\mathbf{x}_B, \lambda \in [0,1] \quad (1)$$

Per crossover event, the mixing parameter, λ, is a randomly generated number in the range [0,1]. Examples of crossover for different values of λ are given in Figure 5.3. Colors are analogous to values, and the mixture of color in the offspring denotes the mixing of values to create the offspring in the fashion of (1). For $\lambda < 0.5$, odd and even-numbered loci are dominated by the behavior of parent B (more red) and A (more yellow) respectively. For $\lambda > 0.5$, this relation is swapped.
All MTBE calculations utilized $N_\ell = 6$ terms in the spherical harmonics expansion of the electron velocity space, all collisions were scattered isotropically, and the gas temperature was set to 300 K. The presence of excited states was neglected; gas kinetics

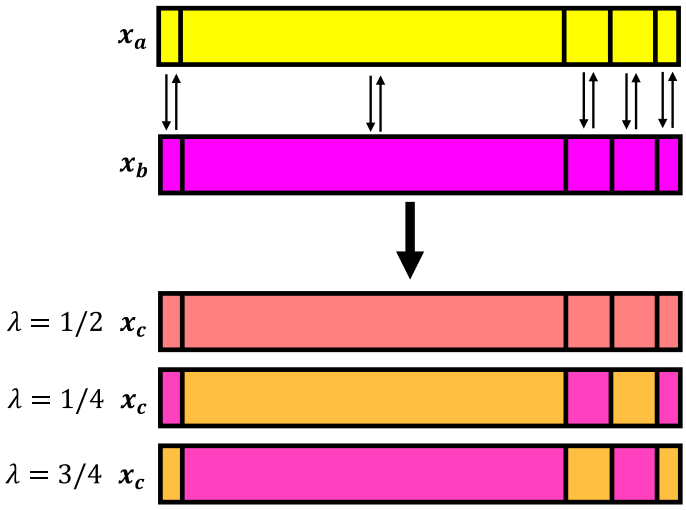

Figure 5.3. Examples of four-point crossover procedures using different values of the mixing parameter λ. *Figure source*: [61].

are insensitive to superelastic collisions at the *E/N* used for this work. Calculations in N_2 and CO_2 mixtures utilized renormalized (see Appendix A) versions of the Biagi v8.97 cross-section set, available on the LXCat database [106,107]

5.2.1.1. Parameterized cross-section set

Each chromosome of **x** was assigned a value that controls one parameter of the cross-section set. The parameterized cross-section sets composed in this way used a genome of m = 23 chromosomes total.

For the GA procedure, the elastic momentum transfer cross-section was constructed as a sum of cubic B-splines. This procedure is given more detail later in section 2.1.2. The attachment cross-section was taken as the Gaussian sum given by Chachereau *et al.* [67], with an additional linear scaling factor of ±20% subject to GA optimization. Note that this differs from the set of attachment cross-sections reported later in section 3, which complements the finalized set with curves for dissociative electron attachment. The experimental ionization cross-sections of Ranković *et al.* [78] were used similarly and also given a GA-optimized linear scaling coefficient of ±20%. For $\varepsilon >$ 100 eV, each ionization cross-section was extrapolated via the calculated shape of Xiong *et al.* [64].

Vibrational and electronic excitation cross-sections were composed as plane wave Born (PWB) approximations [81]. Electronic excitations were given a "BE" scaling (i.e. scaled by $\propto \varepsilon/(\varepsilon + E + B)$ where E is the transition energy of the collision and B is the binding energy of the molecule). Details for individual vibrational and electronic transitions were gathered from IR and UV

experimental data [63,66]. The PWB size and shape parameters for each cross-section, α and f, were subject to GA optimization.

5.2.1.2. Cubic B-spline composition

The elastic momentum transfer cross-section was constructed as a B-spline composition of $N_B = 10$ cubic ($k = 4$) splines in the range of $10^{-1} - 2 \cdot 10^2$ eV defined on an ascending knot sequence $\mathbf{t} = \{t^{(1)}, t^{(2)}, \ldots t^{(NB+k)}\}$ drawn first in a log-log scale and dubbed $S(x)$.

$$S(x) = \sum_{j=1}^{N_B} B_k^{(j)}(x) a^{(j)} \quad \text{for } x \in [-1,2] \tag{2a}$$

$$\sigma_m(\varepsilon) = 10^{S(x)}\ \text{m}^2 \qquad \text{for } \varepsilon = 10^x\ \text{eV} \tag{2b}$$

Each spline $B_k^{(j)}(x)$ is nonzero solely within the range $[t^{(j)}, t^{(j+k)}]$ and normalized.

$$\sum_{j=1}^{N_B} B_k^{(j)}(x) = 1 \quad \text{for } x \in [-1,2] \tag{3}$$

The size of each spline was weighted by one of ten coefficients $a^{(j)}$ given by the chromosomes $\{x^{(2)}, x^{(3)}, \ldots x^{(11)}\}$. To enforce realistic sizes, coefficients for splines located at lower eV were allowed larger values, while splines at higher eV were allowed smaller values. Post-interpretation, values that are mapped logarithmically in the span between 10^{-22} m^2 and 10^{-17} m^2. It is enforced that both the head and tail of $\mathbf{t}$ are made of k duplicate knots so that the curve is non-zero at both extremes.

Spline curvature is additionally controlled by the non-uniform placement of the six inner (non-duplicate) knots. The placement of these knots is controlled by divvying out proportions of the distance between the extreme ends (-1 and 2, respectively), controlling the spacing size according to chromosome value. The adjusted chromosome sequence of seven inter-knot spacings ($\hat{\boldsymbol{x}}_t$) is created by linearly mapping $\mathbf{x}_t = \{x^{(12)}, x^{(13)}, \ldots x^{(18)}\}$ in the range [0.001,0.999] (to prevent any extra duplicate knots) and normalizing such that $\Sigma \hat{\boldsymbol{x}}_t = (1 - -2) = 3$ (to prevent any knots from being placed outside the range). The location of the j^{th} knot in the log-log range is then found using the following procedure.

$$t^{(j)} = -1 \qquad \text{for } j \in [1,2,\ldots k]$$

$$t(j) = t(j-1) + \hat{\boldsymbol{x}}_t{}^{(j-k)} \qquad \text{for } j \in [k+1, k+2, \ldots NB]$$

$$t^{(j)} = 2 \qquad \text{for } j \in [N_B+1, N_B+2, \ldots N_B+k]$$

The above procedure enforces that knots are always placed in ascending order.

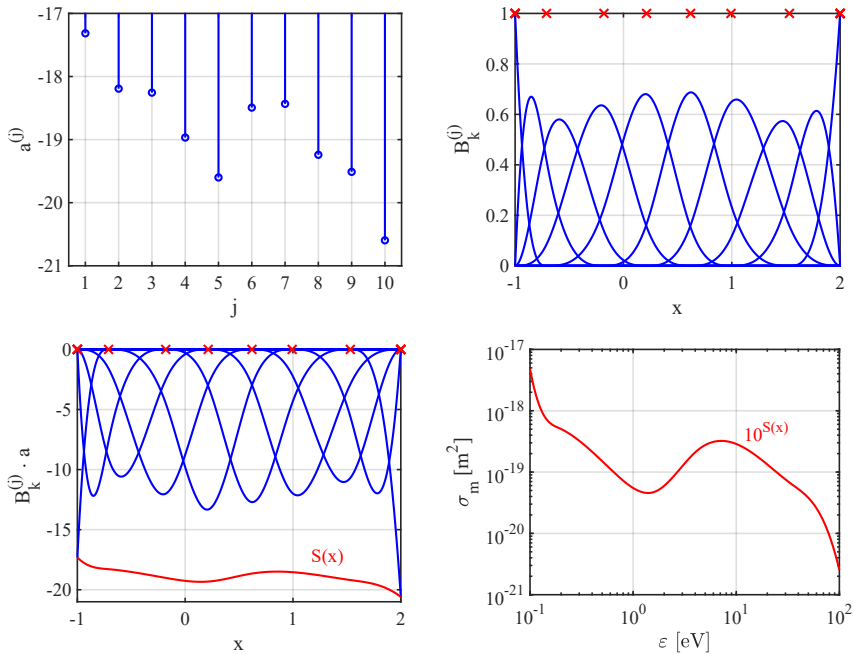

Figure 5.4. B-spline construction of an example elastic momentum transfer cross-section. Top-left: (—◦) coefficients $a^{(j)}$. Top-right: (—) Unweighted normalized cubic (k = 4) splines $B_k^{(j)}(x)$. Knots placed at x = −1 and x = 2 have a multiplicity of four. (×) Knots t. Bottom-left: (—) Weighted splines $B_k^{(j)}(x)a^{(j)}$. (×) The same knots as given in the top-right. (—) Sum of all splines $S(x)$. Bottom right: (—) The elastic momentum transfer cross-section interpreted from $S(x)$. *Figure source*: [61].

With this, $S(x)$ is transformed into $\sigma_m(\varepsilon)$ via (2b).
The use of cubic B-splines for the construction of an example elastic momentum transfer cross-section is demonstrated in Figure 5.4. Non-uniform knot spacing allows each contributing spline to have different curvature, some wider or thinner than others. When knots are placed closer together, curvature may be steeper. The multiplicity of knots at the edge of the curve enforces that the edges of the final cross-sections are never zero.

5.2.1.3. High performance computing implementation

The use of the MTBE creates a relatively expensive fitness function, and the GA procedure requires parallelization to be completed in a timely manner.
Firstly, the GA framework used to conduct this work was implemented independently in MATLAB including capability for both serial and parallel completion of the fitness function (i.e., requiring one process per individual per generation). The fitness function for this work was conducted by composing an argument string which was then passed to a compiled MultiBolt

binary executable. The argument string calls for calculating swarm parameters in a sweep of *E/N* values in a certain C_4F_7N mixture, allowing MultiBolt's internal parallelization (using OpenMP) to further parallelize the sweeps using available cores. The millions of high-resolution MTBE calculations necessary for this work are expedited using multi-core and multi-nodal computation with the help of the Texas Tech University High Performance Computing Center (TTU HPCC). The allocation of 8 nodes, with 32 cores each, sufficed for this work. Note that the number of cores requested per-node can create a significant bottleneck in the efficient scheduling of high performance computing resources.

The final instance of GA evolution which created the cross-sections which appear in this work, ultimately, represented up to two weeks of real-time work scheduled on the HPCC. Per the experience of this work, this represents the time required to generate a cross-section set of acceptable quality once hyper parameters are well-understood. Much more computation time was dedicated to the conduction of the many GA trials required to develop the framework, optimize GA hyper parameters, and fine-tune procedures for cross-section composition.

5.2.2. R-matrix method

This section discusses calculating elastic momentum transfer, vibrational excitation, electronic excitation, and dissociative electron attachment cross-sections using the R-matrix method via QEC [40]. For a more detailed review of the R-matrix method in general, see [65].

The R-matrix method divides the electron-molecule system into two regions: (1) a spherical "inner-region" centered on the target molecule's center of mass which contains the target molecule's wave function in the fixed nuclei approximation, and (2) an "outer-region", beyond this sphere, which contains only the wave function of the scattering electron. The R-matrix defines the boundary between these two regions. QEC first solves for the inner-region wave function and constructs the R-matrix based on this solution. The outer-region wave function is then solved by successively updating the R-matrix at increasing radii from the inter-region boundary to the asymptotic (Coulomb-force governed) region. The wave function for target states is generated using Gaussian type orbitals (GTOs) generated according to either Hartree–Fock (HF) theory or that of multi-configuration self-consistent field (MCSCF).

Calculations of elastic momentum transfer, vibrational excitation, and dissociative attachment cross-sections used a static exchange with polarization (SEP) model. Calculations of electronic excitation cross-sections used a close coupling (CC) model instead, with an active space of eight electrons. Results were found to converge for active spaces of six and seven electrons.

The cc-pVDz basis set [66] was used to calculate elastic momentum transfer, dissociative electron attachment, and electronic excitation cross-sections. The 3-21G basis set [67] was used to calculate vibrational excitation cross-sections. In both cases, the inter-region boundary was set to a radius of 10 Bohr.

The vibrational mode of each dissociative electron attachment collision was estimated as 1000 cm^{-1}. Details for six attachment collisions were taken from [18]. The dissociation energy for each collision was $\varepsilon_D = \varepsilon_n + \varepsilon_{aff}$, where ε_{aff} was the electron affinity for the anion fragments and ε_n is the threshold energy of the collision. Values for the fragments CN- and F- are, from NIST [68], 3.401 eV and 3.862 eV, respectively. Values for the remaining fragments C_4F_6N- and C_4F_3N- are estimated as ε_{aff} = 2.0 and 2.5 eV, respectively; larger molecules generally have lower

electron affinities, and thus the fragments were estimated to have affinities larger than that of the parent anion C_4F_7N- (1.74 eV [62]).

5.3. Results

In this section, the cross-sections achieved by GA evolution, QEC calculations, and those available in the literature are combined and adjusted to form a complete and consistent set. The confidence of GA cross-sections based on the electron energy range is briefly discussed. Swarm parameter calculations in pure C_4F_7N as well as N_2, CO_2, and Ar mixtures are given. Critical field strength calculations for N_2 and CO_2 mixtures are also provided. The finalized set is given in figures 8-11.
While the GA optimization procedure utilized renormalized (see Appendix A) versions of the Biagi cross-sections for carrier gases, swarm calculations reported in this section only utilize the original sets.

5.3.1. Genetic algorithm confidence

Evolution was conducted successfully for ten separate GA sessions, each using a total population of 128 individuals. Each GA session converged within approximately 500 generations. Approximately 80 interesting candidates, out of a combined total population of 1280, were achieved.
The state of the total population at the time evolution was ceased, given in Figure 5.5, yields information about the ability of the population to converge. From Figure 5.5, colors for all chromosomes are random and disorganized for all chromosomes for the least-fit individuals. Chromosomes with low variance are those which are the most relevant for making a fit genome. In this case, chromosomes for some eV ranges of the elastic momentum transfer cross-section have the lowest variance, and chromosomes for vibrational and electronic excitation cross-sections have moderate variance. Some chromosomes, such as #1-3, have high variance even for the best 100 individuals.
The extent to which candidate cross-section sets with similar fitness agree with each other, and for what range of electron energies, is demonstrated in Figure 5.7. Sets of elastic momentum transfer (blue), vibrational excitation (green) and electronic

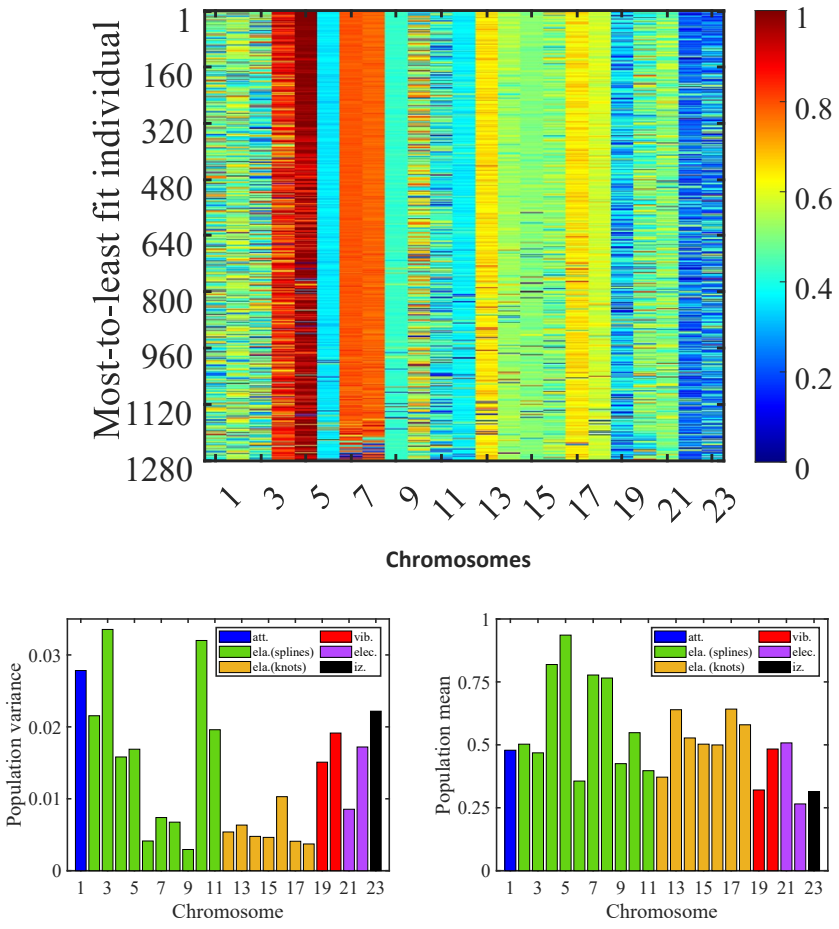

Figure 5.5. State of total population at the time evolution was ceased. (Top) Each individual ranked in order of fitness. Chromosome values are given by color. (Bottom, left) Variance per-chromosome of total population, colored according to relevance to a type of cross-section. organized by-row according to fitness. (Bottom, right) The same for the mean values per-chromosome of the total population. *Figure source*: [105].

excitation (yellow) are given following the same color-shading convention as given previously in Figure 5.6. The most-fit (darkest) region for evolved elastic momentum transfer cross-sections is thin (more confident) between 1 − 50 eV and wide (less confident) for electron energies outside this range. In contrast, the highest-fitness region for both vibrational and electronic excitation is wide for all electron energies.

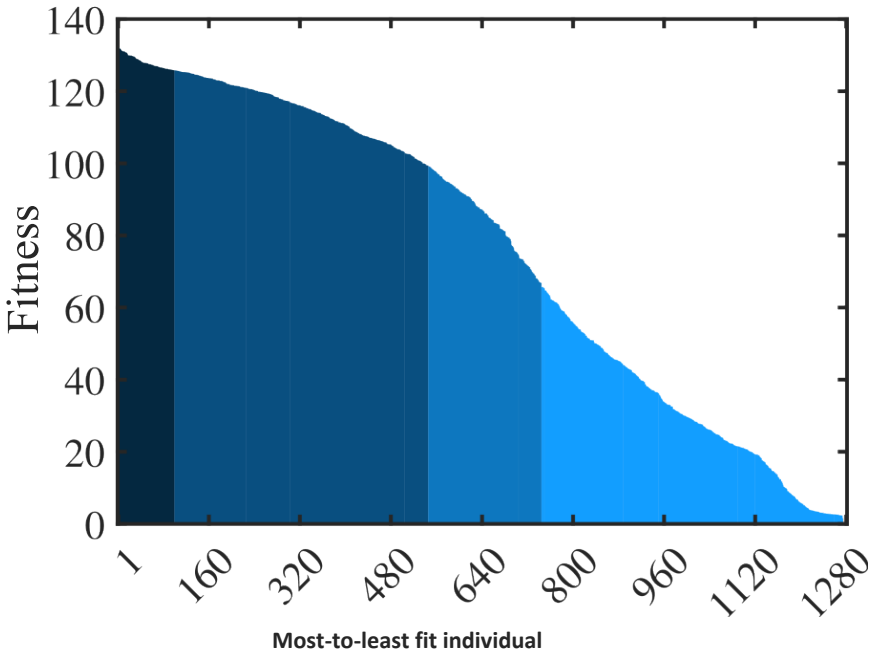

Figure 5.6. Fitness of all individuals in the final total population. The shaded regions, from darkest to lightest, mark sets with fitness within 5% (similar to best), 25% (acceptable), and 50% (physically reasonable) of the best-found, with the lightest region representing all others (poorer behaved or non-physical) present in the population at the time evolution has ceased. *Figure source*: [113].

This suggests that calculations of W, for this work, were insensitive to both vibrational and electronic excitation but very sensitive to elastic momentum transfer between 1 − 50 eV.

5.3.2. Generated and calculated cross-sections

In this section, the cross-sections which compose the sets of elastic momentum transfer, vibrational excitation, electronic excitation, and electron attachment reported in the final set are given.

5.3.2.1. Elastic momentum transfer

Elastic momentum transfer cross-sections are compiled for comparison in Figure 5.8. The curve belonging to the best-fit set in the GA procedure features a local maximum near $\sigma(\varepsilon = 20\text{ eV}) = 3{\cdot}10^{-19}\text{ m}^2$ and a local minimum near $\sigma(\varepsilon = 4.7\text{ eV}) = 1{\cdot}10^{-19}\text{ m}^2$. The

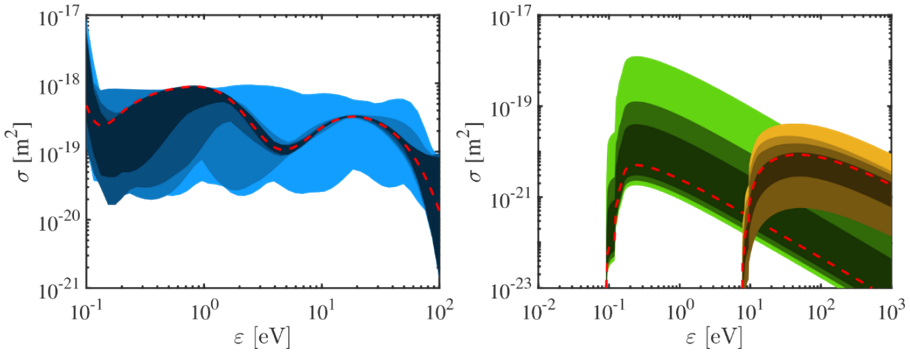

Figure 5.7. Regions of fitness for evolved cross-sections. Regions are colored according to the fitness of results in the same fashion as in figure (6). (Top) (■) elastic momentum transfer cross-sections drawn via B-spline composition. (Bottom) (■) total vibrational and (■) total electronic excitation cross-sections. For each type of collision, the curve belonging to the most-fit set is given as (- - - -). *Figure source*: [113].

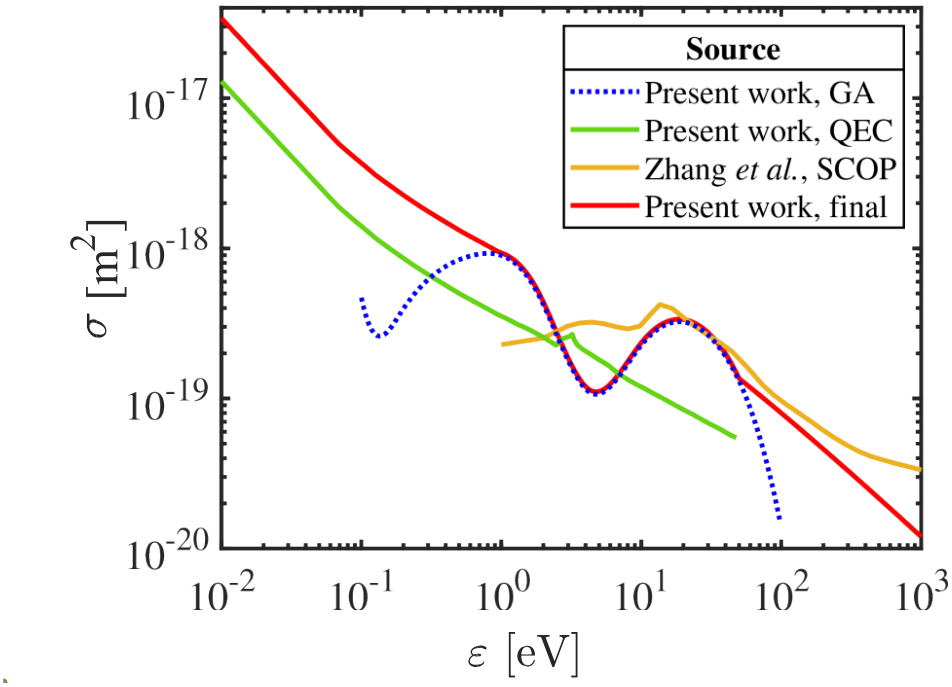

Figure 5.8. Elastic momentum transfer cross-sections for C_4F_7N. (——) R-matrix calculations and (·····) GA optimization. (——) the curve as is reported in the finalized cross-section set. Compared with (——) the SCOP calculated cross-section of Zhang *et al.* [70]. *Figure source*: [113].

curve for the elastic momentum transfer cross-section calculated instead by QEC is given in green. Data calculated in this way is generally reliable up to a region near the first electronic excitation energy [115]; for this work, data of this curve was discarded for $\varepsilon > 10$ eV.

The GA-optimized elastic momentum transfer cross-section was selected for the finalized set. The region between 1–50 eV was maintained as high-confidence curvature. For $\varepsilon <$ 1 eV, the curve was replaced with the shape of the R-matrix elastic momentum transfer calculation. For $\varepsilon > 50$ eV, the curve was replaced with a Born-type extrapolation (i.e. $\propto \log(\varepsilon)/\varepsilon$). Curvature at high ε is most relevant for matching data at high field strengths (such as that of Vemulapalli and Franck [116]), explored in Appendix B.

5.3.2.2. Vibrational excitation

Thirty distinct vibrational collisions were identified via R-matrix calculations. Seven cross-sections whose threshold energies ε_n overlap vibrations identified by [18] were kept as individual and separate collisions. All other curves were summed into a total vibrational cross-section with a low threshold energy of $\varepsilon_n = 0.044$ eV. The set of vibrational cross-sections compiled in this way was scaled (reduced) as necessary to achieve reasonable agreement with experimental swarm data and so that the size of the total vibrational cross-section was reasonable in comparison to the elastic momentum transfer cross-section near the resonance peaks.

The set of vibrational excitation cross-sections composed in this way is depicted in Figure 5.9. Most curves feature two resonances which peak at 1.9 and 2.8 eV. Below 1 eV and above 5 eV, most curves obey a trend of $\propto 1/\varepsilon$.

5.3.2.3. Electronic excitation

Born-corrected electronic excitation cross-sections were calculated via QEC for five singlet-state and six triplet-state excitations from the ground state of C_4F_7N. Depending on the state, data calculated by the CC method was useful up to some threshold between 16 and 24 eV beyond which data was discarded. Beyond this range, a Born-type ($\propto \log(\varepsilon)/\varepsilon$) extrapolation was applied to each cross-section for singlet-state transitions [117]. An empirical $\propto 1/\varepsilon^2$ extrapolation was applied to the triplet-state transitions instead; the probability of optically forbidden transitions is expected to be smaller than that of optically allowed transitions for most eV. For the construction of the final set reported in this work, each electronic excitation cross-section was scaled (increased) as necessary to fulfill k_{eff}/N.

The set of electronic excitation cross-sections is depicted in Figure 5.10. Behavior near the thresholds features peaks and troughs in both singlet and triplet-state transitions.

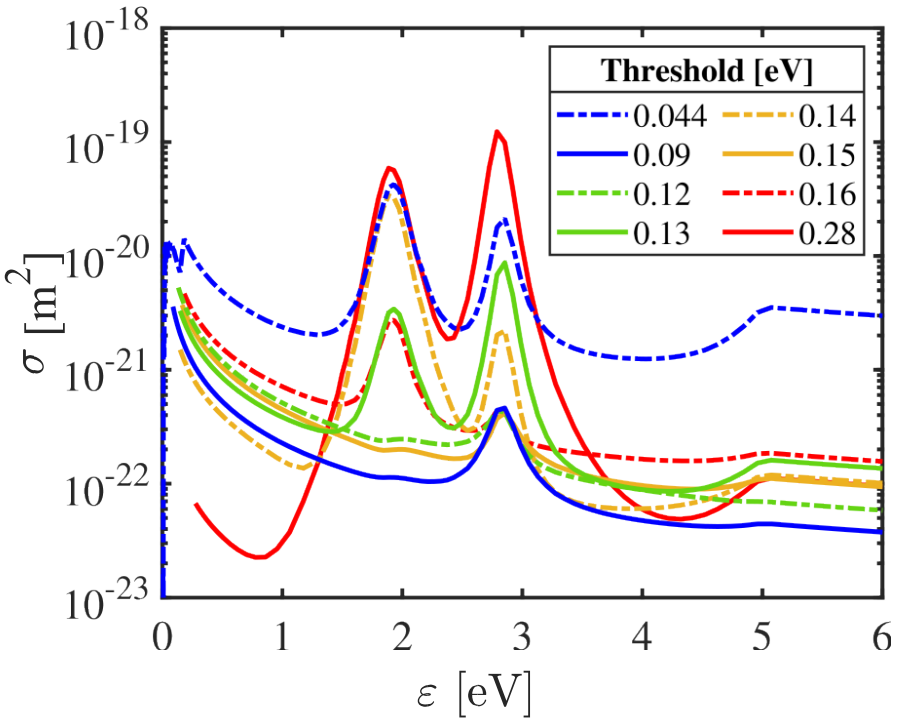

Figure 5.9. Vibrational excitation cross-sections for C_4F_7N. Curves are distinguished by threshold energy. Cross-sections with threshold energies ε_n >= 0.09 eV are individual processes given in more detail in table 1. The cross-section for ε_n = 0.044 eV is a sum of the remaining 23 vibrations calculated by QEC scaled in the same manner as the rest of the set. *Figure source*: [113].

5.3.2.4. Attachment

Six dissociative electron attachment cross-sections for the collisions identified from [18] were calculated via QEC and scaled (reduced) as necessary to fulfill k_{eff}/N. The resultant set is given in Figure 5.11. All collisions share two resonances which peak at 3.2 and 13.9 eV, respectively. In some curves, a separate peak at 9.83 eV becomes distinct from the latter.

No combination of the QEC-calculated and Gaussian-based attachment shapes from Chachereau *et al.* [23], as was available for this work, could achieve consistency to k_{eff}/N in both pure C_4F_7N and N_2 and CO_2 mixtures between 2% and 40% C_4F_7N. No such difficulties were found for Ar mixtures. For this work, the calculation of swarm parameters in pure C_4F_7N and the 4% C_4F_7N, 96% CO_2 mixture was prioritized based on the mixture's prevalence in C_4F_7N industrial applications (i.e. g3 [3]). For these priorities, the best consistency was achieved by including the set of attachment cross-

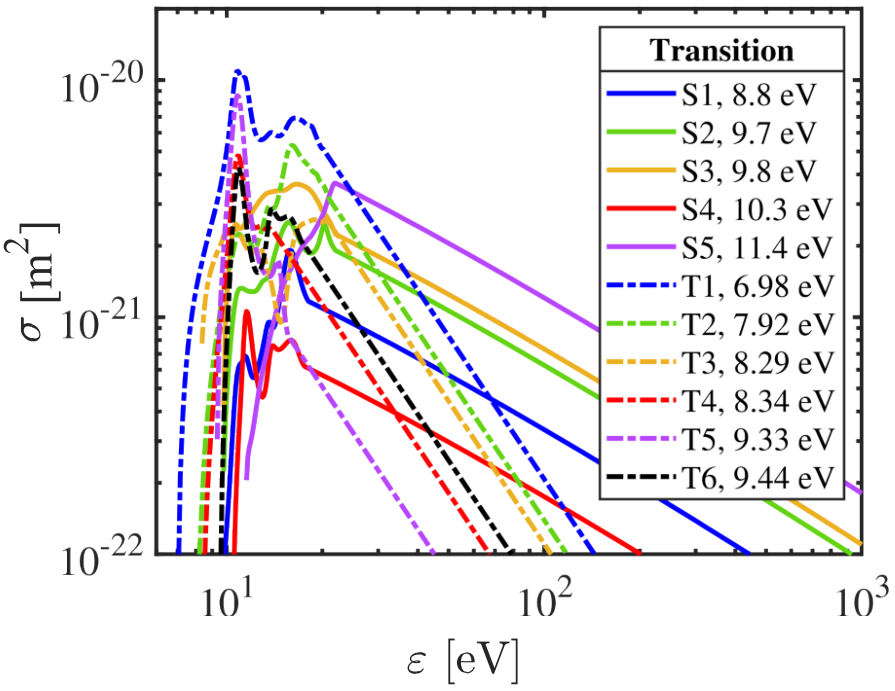

Figure 5.10. Electronic excitation cross-sections for C_4F_7N. (——) Singlet-state transitions. (— · —) Triplet-state transitions. *Figure source*: [69].

sections given in Figure 5.11 as well as an adjustment to the Gaussian sum given by Chachereau *et al.* [111] in which the size of the smaller Gaussian (which peaks near 0.6 eV) is reduced. This curve is here attributed to the "parent" attachment which produces C_4F_7N- and given, in blue, in Figure 5.12.

5.3.2.5. Finalized cross-section set

The cross-sections developed through this work are combined with the complete set of partial ionization cross-sections given by Ranković *et al.* [108] (extrapolated in the manner discussed previously in section 2.1.1). The final complete and consistent cross-section set is given in Figure 5.12. Curves for dissociative attachment, vibrational excitation, electronic excitation, and ionization are given as totals (i.e., sums of all processes). Table 1 lists the individual cross-sections which are present in the finalized set. Curves for individual processes are given in the previous figures 8-11.

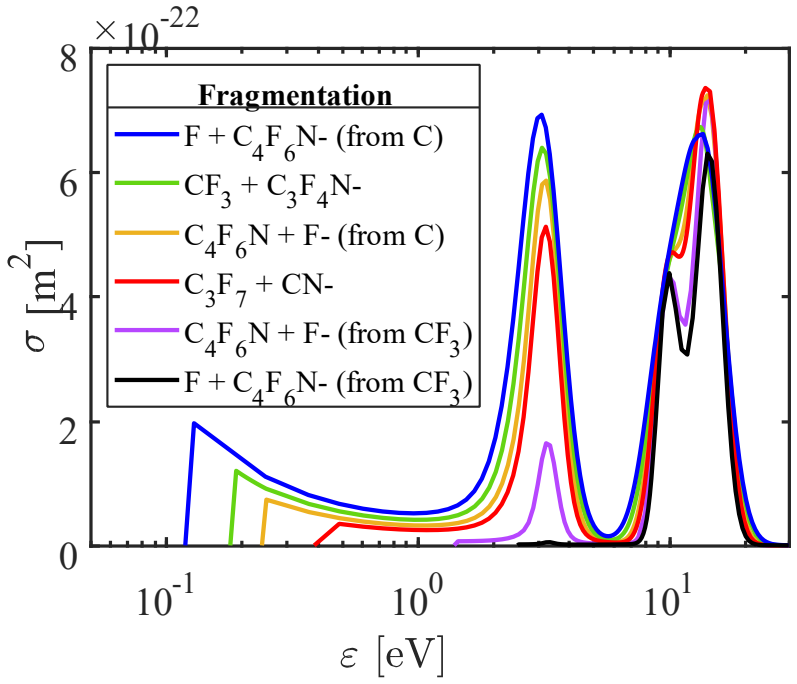

Figure 5.11. Dissociative electron attachment cross-sections for C_4F_7N. Curves are distinguished by fragmentation pattern. *Figure source*: [113].

5.3.3. Calculated swarm parameters

Swarm parameters were calculated using the finalized cross-section set and compared with experimental data in N_2, CO_2, and Ar mixtures and pure C_4F_7N in figures 5.13-5.16. Calculations were made using the same MTBE and settings as discussed previously in section 2.1. Calculations in mixtures used the Biagi cross-section sets for the carrier gases N_2, CO_2, and Ar as are available on the LXCat database [106,107] (note that the renormalized sets described in Appendix A are not used for any calculations in this section).
For the bulk drift velocity W and bulk longitudinal diffusion coefficient D_LN, results achieved were within the visible experimental error of Chachereau *et al.* [67]. The average error between calculations and experimental data was within 16%, 2%, and 19% for k_{eff}/N, W and D_LN for pure C_4F_7N. In mixtures, error in W was contained to within 3% for all cases, and error in D_LN was likewise within 21%. In all these cases, the error

Table 5.1: List of collisions included in the set. Adjustments denoted as follows: (∗) Curve is scaled. (†) Curve is extrapolated. (††) Curve is adjusted in some other way, see notes. *Table source*: [69].

#	Source	Attachment collision	ε_n [eV]	Notes
1	[23]††	$e + C_4F_7N \rightarrow C_4F_7N-$	0	Sum of Gaussians. Gaussian #2 is smaller.
2	QEC*	$e + C_4F_7N \rightarrow F + C_4F_6N^-$	0.12	Dissociation from C
3	QEC*	$e + C_4F_7N \rightarrow CF_3 + C_3F_4N^-$	0.18	-
4	QEC*	$e + C_4F_7N \rightarrow C_4F_6N + F^-$	0.24	Dissociation from C
5	QEC*	$e + C_4F_7N \rightarrow C_3F_7 + CN^-$	0.39	-
6	QEC*	$e + C_4F_7N \rightarrow C_4F_6N + F^-$	1.4	Dissociation from CF_3
7	QEC*	$e + C_4F_7N \rightarrow F + C_4F_6N^-$	2.5	Dissociation from CF_3

#	Source	Elastic momentum transfer collision	m_e/M	Notes
8	GA†, QEC*	$e + C_4F_7N \rightarrow e + C_4F_7N$	2.81e-6	-

#	Source	Vibrational excitation collision	ε_n [eV]	Notes
9	QEC*	$e + C_4F_7N \rightarrow e + C_4F_7N$(v*, sum)	0.0044	Sum of other vib. levels
10	QEC*	e + C4F7N →e + C4F7N(v*, CF3-AsymUmbr)	0.09	-
11	QEC*	$e + C_4F_7N \rightarrow e + C_4F_7N$(v*, CF-stretch(1))	0.12	-
12	QEC*	$e + C_4F_7N \rightarrow e + C_4F_7N$(v*, CF-stretch(2))	0.13	-
13	QEC*	$e + C_4F_7N \rightarrow e + C_4F_7N$(v*, CF-stretch(3))	0.14	-
14	QEC*	$e + C_4F_7N \rightarrow e + C_4F_7N$(v*, CC-stretch(1))	0.15	-
15	QEC*	$e + C_4F_7N \rightarrow e + C_4F_7N$(v*, CC-stretch(2))	0.16	-
16	QEC*	$e + C_4F_7N \rightarrow e + C_4F_7N$(v*, CN-stretch)	0.28	-

#	Source	Electronic excitation collision	ε_n [eV]	Notes
17	QEC*†	$e + C_4F_7N \rightarrow e + C_4F_7N$(e*, T_1)	6.98	-
18	QEC*†	$e + C_4F_7N \rightarrow e + C_4F_7N$(e*, T_2)	7.92	-
19	QEC*†	$e + C_4F_7N \rightarrow e + C_4F_7N$(e*, T_3)	8.29	-
20	QEC*†	$e + C_4F_7N \rightarrow e + C_4F_7N$(e*, T_4)	8.34	-
21	QEC*†	$e + C_4F_7N \rightarrow e + C_4F_7N$(e*, S_1)	8.8	-

22	QEC*†	$e + C_4F_7N \rightarrow e + C_4F_7N(e^*, T_5)$	9.33	-
23	QEC*†	$e + C_4F_7N \rightarrow e + C_4F_7N(e^*, T_6)$	9.44	-
24	QEC*†	$e + C_4F_7N \rightarrow e + C_4F_7N(e^*, S_2)$	9.7	-
25	QEC*†	$e + C_4F_7N \rightarrow e + C_4F_7N(e^*, S_3)$	9.8	-
26	QEC*†	$e + C_4F_7N \rightarrow e + C_4F_7N(e^*, S_4)$	10.3	-
27	QEC*†	$e + C_4F_7N \rightarrow e + C_4F_7N(e^*, S_5)$	11.4	-

#	Source	Ionization collision	ε_n [eV]	Notes
28	[36]†	$e + C_4F_7N \rightarrow e + e + C_3F_4N + CF^+_3$	11.9	Extrap.: Xiong *et al.* [64]
29	[36]†	$e + C_4F_7N \rightarrow e + e + CF_4 + C_3F_3N^+$	14.7	Extrap.: Xiong *et al.* [64]
30	[36]†	$e + C_4F_7N \rightarrow e + e + F + C_4F_6N^+$	16.1	Extrap.: Xiong *et al.* [64]
31	[36]†	$e + C_4F_7N \rightarrow e + e + C_2F_5 + C_2F_2N^+$	18.4	Extrap.: Xiong *et al.* [64]
32	[36]†	$e + C_4F_7N \rightarrow e + e + C_3F_4N + F_2 + CF^+$	21.0	Extrap.: Xiong *et al.* [64]
33	[36]†	$e + C_4F_7N \rightarrow e + e + C_2F_3N + C_2F_4^+$	24.1	Extrap.: Xiong *et al.* [64].
34	[36]†	$e + C_4F_7N \rightarrow e + e + C_3F_5N + CF_2^+$	25.6	Extrap.: Xiong *et al.* [64]
35	[36]†	$e + C_4F_7N \rightarrow e + e + C_2F_6 + C_2FN^+$	28.2	Extrap.: Xiong *et al.* [64]

between the calculations and experiment was within the spread of the reported data. For N_2 and CO_2 mixtures with less than 10% C_4F_7N, the average error between the calculations and the experimental data was typically within 20% for k_{eff}/N. For increasing C_4F_7N, the error was as large as 75% in the 40% C_4F_7N mixtures. Values and curvature of k_{eff}/N were well met for pure C_4F_7N and for mixtures of less than 10% C_4F_7N content. The curvature remains acceptable for other mixtures, but the attachment is too large overall for mixtures closer to 40% C_4F_7N.

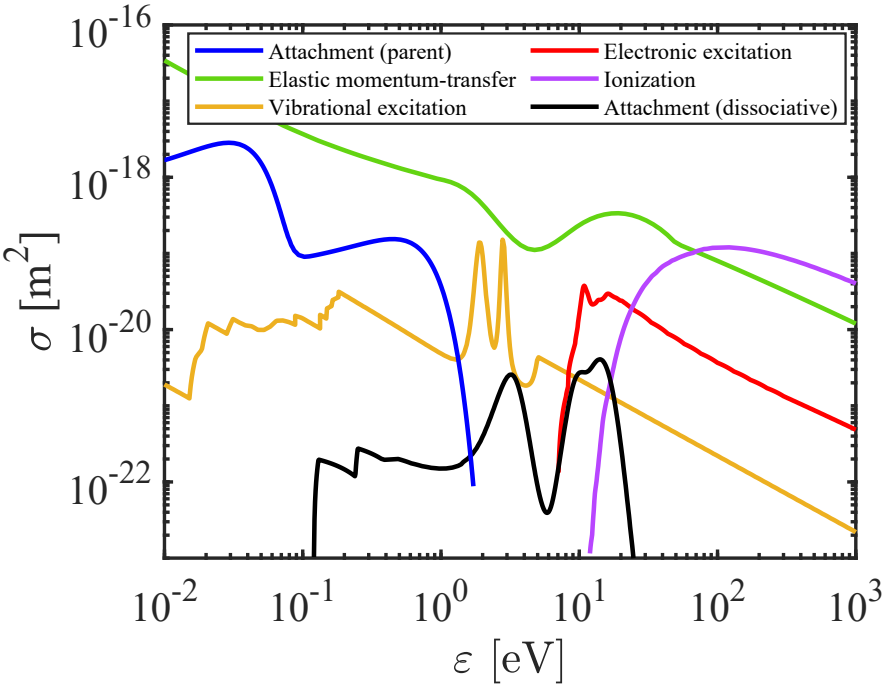

Figure 5.12. The set of finalized C_4F_7N cross-sections. (—) Parent attachment. (—) elastic momentum transfer. Curves for (—) dissociative electron attachment, (—) vibrational excitation, (—) electronic excitation, and (—) ionization are totals. *Figure source*: [69].

Calculations of the critical field strength $(E/N)_{crit}$ (i.e. E/N such that $\alpha_{eff}/N = 0$) are given in Figure 5.17. The critical field strength is found to be 971 Td in pure C_4F_7N, similar to the average value of other reports and closest to that reported by Chachereau *et al.* [67]. Other reports in pure C_4F_7N differ from this value by ±3%. Results for mixtures in-general were acceptable and best fit data in both mixtures for less than 20% C_4F_7N content.

5.4. Conclusions

A complete and consistent set of electron-neutral collision cross-sections for C_4F_7N was developed. A genetic algorithm procedure, original and unique to this work, which confidently uncovers the curvature of the elastic momentum transfer cross-section and the general size of inelastic cross-sections, was described. A large array of cross-sections for particular electron-C_4F_7N collisions were calculated *ab initio* using the R-matrix method software Quantemol Electron Collisions [84]. The finalized cross-section set was used to calculate electron rate, transport, and growth coefficients as well as critical field

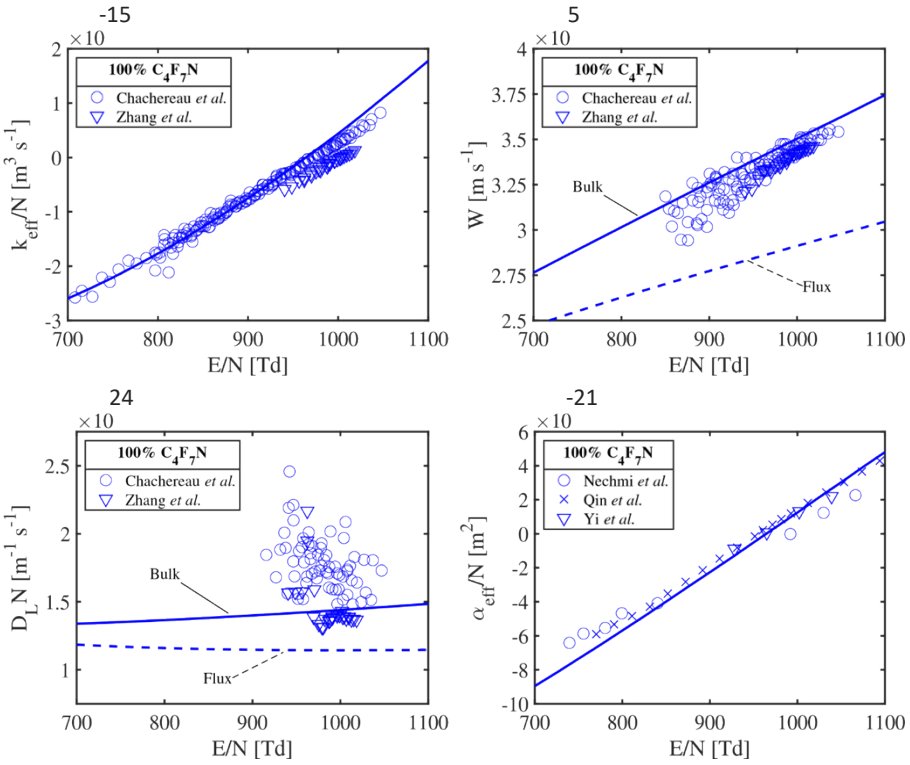

Figure 5.13. Calculated rate, transport, and growth coefficients in pure C_4F_7N. Flux drift velocity and flux longitudinal diffusion coefficients are given as (- - - -) for comparison. Rate and transport coefficients are compared with the pulsed Townsend experimental data of Chachereau *et al.* [23] and Zhang *et al.* [25]. Growth coefficients (the primary Townsend coefficient) are compared with the steady-state Townsend experimental data of (◦) Nechmi *et al.* [27], (△) Yi *et al.* [30], and (×) Qin *et al.* [29]. *Figure source*: [69].

strengths in a wide array of gas mixtures which agree well with data found in the open literature. The authors plan to make the complete cross-section set available to the community on the LXCat project [74,78,79].

The set contains substantial information on the gas chemistry of C_4F_7N and its mixtures. Information on neutral, ion, and anion fragments from dissociative ionization and attachment collisions is included in the set. Neutral dissociation cannot be confidently tied to individual electronic excitations at this time; from Ovad *et al.* [58], this process is likely dominated by fragmentation into CF_3, CN, and the balancing fragments from some electronic singlet-state transitions.

For C_4F_7N modeling in industrial applications, accurate results depend additionally on the accurate modeling of the carrier gas. The set proposed in this work is precise for pure C_4F_7N. Discussion on inabilities to meet electron swarm parameters in mixtures must also consider the

experimental arrangements of the data [118] and cross-sections of carrier gases. Note that the kinetics for high-pressure and long-gap C_4F_7N mixtures requires, additionally, the modeling of electron detachment (i.e. electron-ion collisions). More information on this particular topic may be found elsewhere [24]. The reported set is solely focused on electron-neutral collisions.

The final set's parent attachment cross-section (the blue curve in Figure 5.12 as derived from swarm data and prior literature is of lower confidence than the rest of the set. Future work may concern the uncovering of a higher confidence curvature for this cross-section using additional recent swarm data.

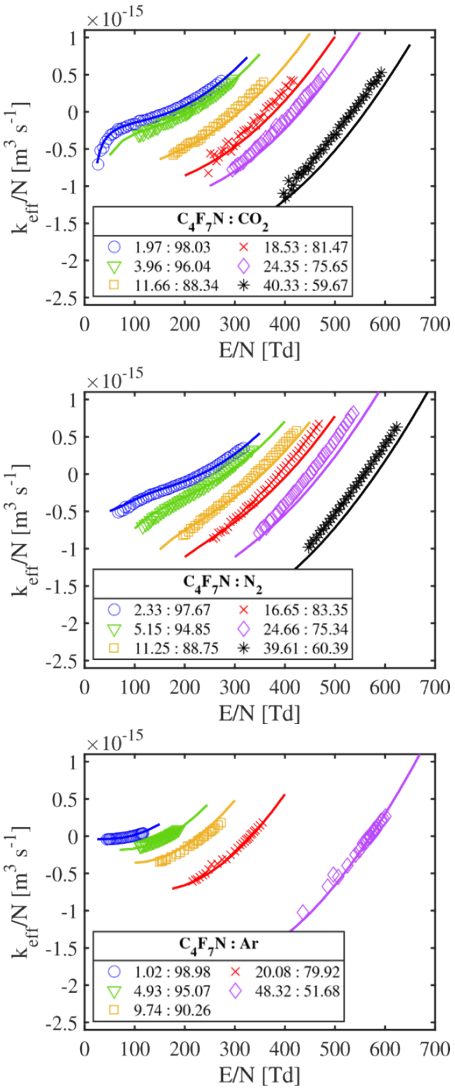

Figure 5.14. Density-reduced effective ionization rate coefficients calculated using the finalized set in N_2, CO_2, Ar, and C_4F_7N mixtures. Mixtures are grouped by color. Colored lines are calculated results. In N_2 and CO_2 mixtures, markers are the pulsed Townsend experimental data of Chachereau *et al.* [23] colored according to the mixture. In Ar mixtures, markers are the pulsed Townsend experimental data of Zhang *et al.* [26] colored according to different mixtures. *Figure source*: [113].

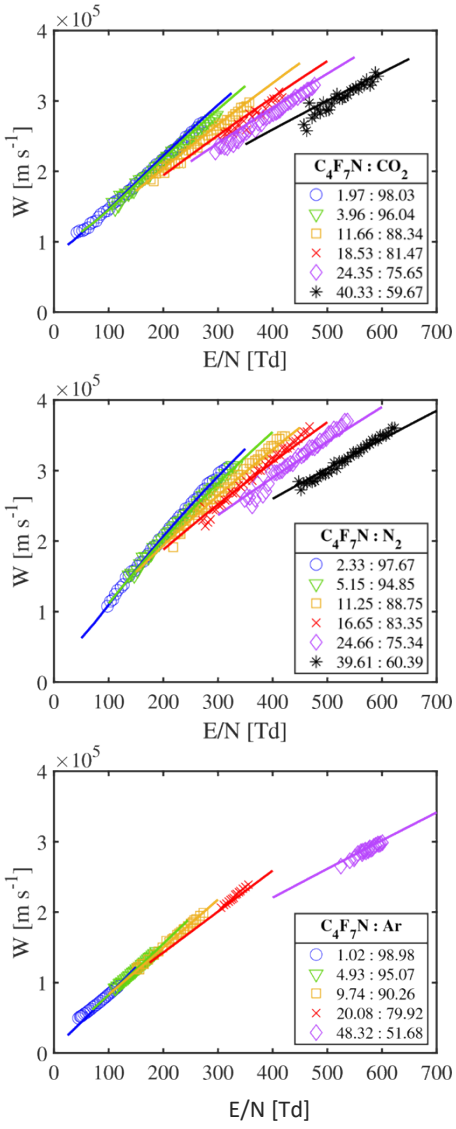

Figure 5.15. Bulk drift velocities calculated in N_2, CO_2, Ar, and C_4F_7N mixtures. The same colors, markers, and data sources as Figure 5.14 are used. *Figure source*: [113].

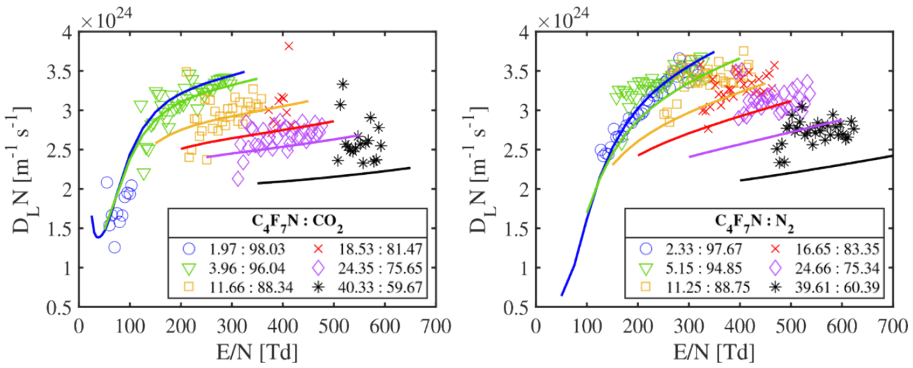

Figure 5.16. Density-reduced bulk longitudinal diffusion coefficients calculated using the finalized set in N_2, CO_2, and C_4F_7N mixtures. The same color and marker convention as Figure 5.14 is used. Calculations in Ar mixtures are not given because data is absent for this coefficient. *Figure source*: [113].

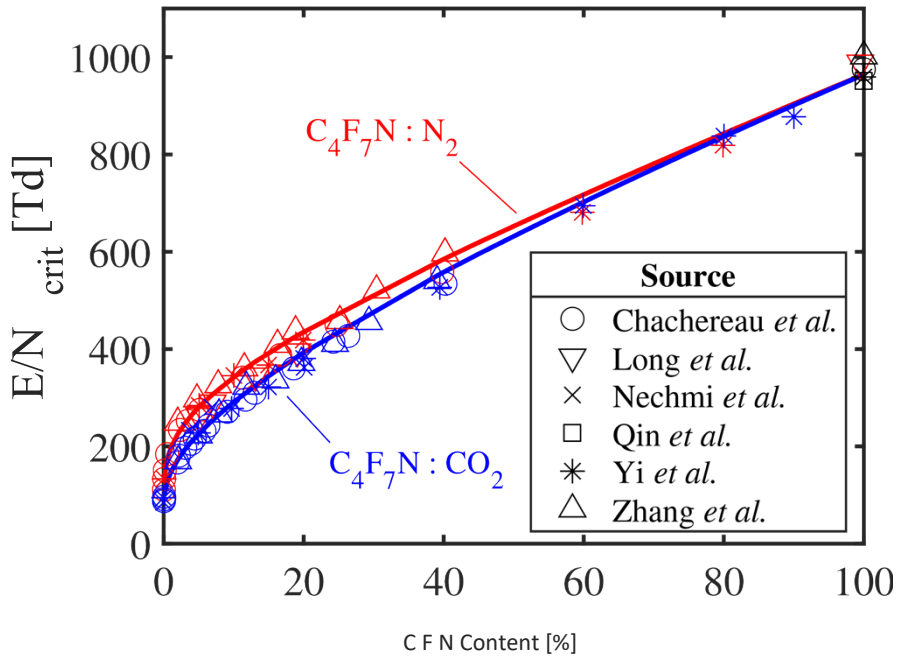

Figure 5.17. Calculated critical field strengths in C_4F_7N mixtures. Compared with the values reported by the experimental data of (◦) Chachereau *et al.* [23], (▽) Long *et al.* [28], (×) Nechmi *et al.* [71], (□) Qin *et al.* [73], (∗) Yi *et al.* [74], and (△) Zhang *et al.* [25]. Lines are calculated results in (——) N_2 and (– –) CO_2 mixtures. Colored markers are in the same mixtures as the lines. Black markers are values reported for pure C_4F_7N. *Figure source*: [113].

REFERENCES

[1] Pan, B. et al., "Green Gas for Grid as an Eco-Friendly Alternative Insulation Gas to SF6: A Review," Applied Sciences, vol. 10, no. 7, 2020. DOI: 10.3390/app10072526

[2] Liu, X. "Best choice of insulation gas medium for MMGS in fast linear transformer driver," AIP Advances, vol. 10, no. 3, 2020. DOI: 10.1063/1.5136275

[3] Kieffel, Y. et al. (2017), "Characteristics of g3 – an Alternative to SF6", 24th International Conference & Exhibition on Electricity Distribution p. 1

[4] Xiao, A. et al. (2019), "Environmentally Friendly Insulating Gases as SF6 Alternatives for Power Utilities", 2nd International Conference on Electrical Materials and Power Equipment p. 42

[5] Chachereau, A., Hösl, A., and Franck, C.M. (2018), "Electrical Insulation Properties of the Perfluoronitrile C4F7N", Journal of Physics D: Applied Physics 51: 495201

[6] Fu, Y. et al. (2019), "Theoretical Study of the Decomposition Mechanism of C4F7N", Journal of Physics D: Applied Physics 52: 245203

[7] Wei, J. et al (2020), "Analysis of Decomposition Products of SF6 and C4F7N under Low Energy Corona Discharge", 2020 Electrical Insulation Conference p. 167

[8] Zhang, B. et al (2020), "Fundamental Physiochemical Properties of SF6-Alternative Gases: A Review of Recent Progress", Journal of Physics D: Applied Physics 53: 173001

[9] Chunlin, W. et al. (2017), "Thermophysical Properties Calculation of C4F7N/CO2 mixture Based on Computational Chemistry—A Theoretical Study of SF6 Alternative", 2017 4th International Conference on Electric Power Equipment p. 255

[10] Li, Y. et al. (2019), "Experimental Study on the Partial Discharge and AC Breakdown Properties of C4F7N/CO2 Mixture", High Voltage 4: 12-17

[11] Xiao, S. et al (2021), "The Sensitivity of C4F7N to Electric Field and Its Influence to Environment-Friendly Insulating Gas Mixture C4F7N/CO2", Journal of Physics D: Applied Physics 54: 055501

[12] André-Maouhoub et al. (2020), "Production of Graphite During the Extinguishing Arc with New SF6 Alternative Gases", Plasma Chemistry and Plasma Processing 40: 795-808

[13] Fu, Y. et al. (2019), "The Decomposition Mechanism of C¬4F7N-Cu Gas Mixtures", AIP Advances 9: 115216

[14] S. Braginskii, "Theory of the Development of a Spark Channel," *Journal of Experimental and Theoretical Physics*, vol. 34, no. 4, pp. 1068–1074, 1958.

[15] T. Martin, J. Seamen, and D. Jobet, "Energy losses in switches," *9th IEEE Pulsed Power Conference,* Albuquerque, NM, June 1993. (DOI: 10.1109/PPC.1993.513375)

[16] J. Pouncey and J. Lehr, "A spark gap model for LTspice and similar circuit simulation software," *2015 IEEE Pulsed Power Conference (PPC)*, Austin, TX, 2015. (DOI: 10.1109/PPC.2015.7296883)

[17] B Zhang et al., "Decomposition characteristics of C4F7N/CO2 mixture under AC discharge breakdown," AIP Advances, vol. 9, no. 11, 2019, https://doi.org/10.1063/1.5115588

[18] Li et al., "Decomposition Properties of C4F7N/N2 Gas Mixture: An Environmentally Friendly Gas to Replace SF6," Industrial & Engineering Chemistry Research, vol. 57, no. 14, pp. 5173-5182 2018, https://doi.org/10.1021/acs.iecr.8b00010

[19] Chen et al., "Decomposition pathway of C4F7N gas considering the participation of ions," Journal of Applied Physics, vol. 128, no. 14, 2020, https://doi.org/10.1063/5.0024646

[20] Ye et al., "Effect of O2 on AC Partial Discharge and Decomposition Behavior of C4F7N/CO2/O2 Gas Mixture," IEEE Transactions on Dielectrics and Electrical Insulation, vol, 28, no. 4, pp. 1440-1448, 2021, https://doi.org/10.1109/TDEI.2021.009626

[21] Ye et al., "Arc decomposition behavior of C4F7N/Air gas mixture and biosafety evaluation of its by-products," High Voltage, vol, 7, no. 5, 856-865, 2022, https://doi.org/10.1049/hve2.12233

[22] X Zhang et al., "Detection of decomposition products of C4F7N-CO2 gas mixture based on infrared spectroscopy," Vibrational Spectroscopy, vol. 110, 2020, https://doi.org/10.1016/j.vibspec.2020.103114

[23] Rankovic et al., "Dissociative ionization dynamics of dielectric gas C_3F_7CN," Physical Chemistry Chemical Physics, vol. 21, no. 30, pp. 16451-16458, 2019, https://doi.org/10.1039/C9CP02188D

[24] Itikawa, "Electron Collisions with Hydrogen Fluoride," Journal of Physical and Chemical Reference Data, vol. 46, no. 1, 2017, http://dx.doi.org/10.1063/1.4976571

[25] A. Lietz, B. Yee, J. Musk II, H. Moffat, D. Wiemann, T. Settecerri, D. Fergenson, M. Omana and M. Hopkins, " Laser-driven ionization mechanisms of aluminum for single particle aerosol mass spectrometry.," *Spectrochimica Acta Part B: Atomic Spectroscopy,* vol. 197, p. 106543, 2022.

[26] L. Zhong, J. Wang, J. Xu, X. Wang and M. Rong, "Effects of buffer gases on plasma properties and arc decaying characteristics of C 4 F 7 N–N 2 and C 4 F 7 N–CO 2 arc plasmas," *Plasma Chemistry and Plasma Processing,* vol. 39, pp. 1379-1396, 2019.

[27] M. Gnybida, C. Rümpler and V. R. T. Narayanan, "Radiative properties and numerical modeling of C4F7N-CO2-O2 thermal plasma," *PLASMA PHYSICS AND TECHNOLOGY,* vol. 6, no. 2, pp. 144-147, 2019.

[28] J. J. Lowke, " Calculated properties of vertical arcs stabilized by natural convection," *Journal of Applied Physics,* vol. 50, no. 1, pp. 147-157, 1979.

[29] M. J. Kushner, R. D. Milroy and W. D. Kimura, "A laser-triggered spark gap model," *Journal of applied physics,* vol. 58, no. 8, pp. 2988-3000, 1985.

[30] S. Bindu, H. A. Mangalvedekar, S. Umbarkar, A. Sharma, D. P. Chakravarti, P. C. Saroj and K. C. Mittal, "Modelling of a spark gap switch," in *IEEE 10th International Conference on the Properties and Applications of Dielectric Materials*, 2012.

[31] L. Chen, B. Zhang, J. Xiong, X. Li and A. B. Murphy, "Decomposition mechanism and kinetics of iso-C4 perfluoronitrile (C4F7N) plasmas," *Journal of Applied Physics,* vol. 126, no. 16, 2019.

[32] Y. Itikawa, "Cross sections for electron collisions with carbon monoxide," *Journal of Physical and Chemical Reference Data,* vol. 44, no. 1, 2015.

[33] V. Tarnovsky, P. Kurunczi, D. Rogozhnikov and K. Becker, "Absolute cross sections for the dissociative electron impact ionization of the CFx (x= 1− 3) free radicals," *International journal of mass spectrometry and ion processes,* vol. 128, no. 3, pp. 181-194, 1993.

[34] A. P. Hickman, "Approximate scaling formula for ion–ion mutual neutralization rates," *The Journal of Chemical Physics,* vol. 70, no. 11, pp. 4872-4878, 1979.

[35] X. Wang, Q. Gao, Y. Fu, A. Yang, M. Rong, Y. Wu, C. Niu and A. Murphy, "Dominant particles and reactions in a two-temperature chemical kinetic model of a decaying SF6 arc," *Journal of Physics D: Applied Physics,* vol. 49, no. 10, p. 105502, 2016.

[36] Franck C M, Chachereau A and Pachin J 2021 *IEEE Electrical Insulation Magazine* **37** 7–16

[37] Rabie M and Franck C M 2018 *Environmental Science & Technology* **52** 369–380

[38] Beroual A and Haddad A M 2017 *Energies* **10** 1216

[39] Loucas G Christophorou James K Olthoff D S G 1997 Gases for electrical insulation and arc interruption: Possible present and future alternatives to pure sf6 Tech. rep.

[40] 2018 3M Novec 4710 insulating gas Electronic URL https://multimedia.3m.com/mws/media/

[41] 1132124O/3m-novec-4710-insulating-gas-tech-data-sheet.pdf

[42] GWP and 3M Novec 4710 insulating gas URL https://multimedia.3m.com/mws/media/

[43] 1511101O/gwp-and-3m-novec-4710-insulating-gas.pdf

[44] Pan B, Wang G, Shi H, Shen J, Ji H K and Kil G S 2020 *Applied Sciences* **10** 2526

[45] Fu Y, Yang A, Wang X and Rong M 2019 *Journal of Physics D: Applied Physics* **52** 245203

[46] Chen L, Zhang B, Li X and Yang T 2020 *Journal of Applied Physics* **128** 143303

[47] Zhang B, Li C, Xiong J, Zhang Z, Li X and Deng Y 2019 *AIP Advances* **9** 115212

[48] Narayanan V R T, Gnybida M and Rümpler C 2022 *Journal of Physics D: Applied Physics* **55** 295502

[49] Wu Y, Wang C, Sun H, Murphy A B, Rong M, Yang F, Chen Z, Niu C and Wang X 2018 *Journal of Physics D: Applied Physics* **51** 155206

[50] Zhong L, Wang J, Xu J, Wang X and Rong M 2019 *Plasma Chemistry and Plasma Processing* **39** 1379–1396

[51] Zheng Y, Yan X, Chen W, Zhou W, Hu S and Li H 2019 *Plasma Research Express* **1** 025013

[52] Xiao S, Gao B, Pang X, Zhang X, Li Y, Tian S, Tang J and Luo Y 2020 *Journal of Physics D: Applied Physics* **54** 055501

[53] Li Y, Zhang X, Zhang J, Xiao S, Xie B, Chen D, Gao Y and Tang J 2019 *Journal of Hazardous Materials* **368** 653–660

[54] Huang, Wang, Liu, Zhang and Zeng 2019 *Processes* **7** 698

[55] Ranković M, P R K T, Nag P, Kočišek J and Fedor J 2020 *The Journal of Chemical Physics* **152** 244304

[56] Bian C, Dai F, Cheng J, Tao J, Tan T and Song Y 2020 The research on infrared spectrum of c4f7n by combined experimental and theoretical study *2020 IEEE 4th Conference on Energy Internet and Energy System Integration (EI2)* (IEEE)

[57] Zhang X, Zhang Y, Huang Y, Li Y, Cheng H and Xiao S 2020 *Vibrational Spectroscopy* **110** 103114

[58] Ovad T, Sapunar M, Sršeň Š, Slavi□ ček P, Maši□ n Z, Jones N C, Hoffmann S V, Ranković M and

[59] Fedor J 2023 *The Journal of Chemical Physics* **158** 014303

[60] Zhang Y, Zhang X, Liu C, Li Y, Cui Z and Fu M 2019 *Applied Spectroscopy* **73** 917–926

[61] Chachereau A, Hösl A and Franck C M 2018 *Journal of Physics D: Applied Physics* **51** 495201

[62] Hösl A, Chachereau A, Pachin J and Franck C M 2019 *Journal of Physics D: Applied Physics* **52** 235201

[63] Zhang B, Xiong J, Hao M, Yao Y, Li X and Murphy A B 2022 *Journal of Applied Physics* **131** 033304

[64] Zhang B, Hao M, Yao Y, Xiong J, Li X, Murphy A B, Sinha N, Antony B and Ambalampitiya H B 2023 *Journal of Physics D: Applied Physics* **56** 134001

[65] Nechmi H, Beroual A, Girodet A and Vinson P 2017 *IEEE Transactions on Dielectrics and Electrical Insulation* **24** 886–892

[66] Long Y, Guo L, Shen Z, Chen C, Chen Y, Li F and Zhou W 2019 *IEEE Transactions on Dielectrics and Electrical Insulation* **26** 1358–1362

[67] Qin Z, Long Y, Shen Z, Chen C, Guo L and Zhou W 2019 *Applied Sciences* **9** 3686

[68] Yi C, Yuan Z, Tu Y, Zhang Y and Wang C 2020 *IEEE Transactions on Dielectrics and Electrical Insulation* **27** 1015–1021

[69] Carbone E, Graef W, Hagelaar G, Boer D, Hopkins M M, Stephens J C, Yee B T, Pancheshnyi S, van Dijk J and Pitchford L 2021 *Atoms* **9** 16

[70] Adamovich I, Baalrud S D, Bogaerts A, Bruggeman P J, Cappelli M, Colombo V, Czarnetzki U, Ebert U, Eden J G, Favia P, Graves D B, Hamaguchi S, Hieftje G, Hori M, Kaganovich I D, Kortshagen U, Kushner M J, Mason N J, Mazouffre S, Thagard S M, Metelmann H R, Mizuno

[71] A, Moreau E, Murphy A B, Niemira B A, Oehrlein G S, Petrovic Z L, Pitchford L C, Pu Y K,

[72] Rauf S, Sakai O, Samukawa S, Starikovskaia S, Tennyson J, Terashima K, Turner M M, van de Sanden M C M and Vardelle A 2017 *Journal of Physics D: Applied Physics* **50** 323001

[73] Christophorou L G and Olthoff J K 2000 *Journal of Physical and Chemical Reference Data* **29** 267–330

[74] Pancheshnyi S, Biagi S, Bordage M, Hagelaar G, Morgan W, Phelps A and Pitchford L 2012 *Chemical Physics* **398** 148–153

[75] Pitchford L C, Alves L L, Bartschat K, Biagi S F, Bordage M C, Bray I, Brion C E, Brunger M J, Campbell L, Chachereau A, Chaudhury B, Christophorou L G, Carbone E, Dyatko N A, Franck

[76] C M, Fursa D V, Gangwar R K, Guerra V, Haefliger P, Hagelaar G J M, Hoesl A, Itikawa Y,

[77] Kochetov I V, McEachran R P, Morgan W L, Napartovich A P, Puech V, Rabie M, Sharma L, Srivastava R, Stauffer A D, Tennyson J, de Urquijo J, van Dijk J, Viehland L A, Zammit M C, Zatsarinny O and Pancheshnyi S 2016 *Plasma Processes and Polymers* **14** 1600098

[78] Ranković M, Chalabala J, Zawadzki M, Kočišek J, Slavı̌ček P and Fedor J 2019 *Physical Chemistry Chemical Physics* **21** 16451–16458

[79] Kim Y K 2007 *The Journal of Chemical Physics* **126** 064305

[80] Crawford O H 1967 *The Journal of Chemical Physics* **47** 1100–1104

[81] Zatsarinny O and Bartschat K 2013 *Journal of Physics B: Atomic, Molecular and Optical Physics* **46** 112001

[82] Cooper B, Tudorovskaya M, Mohr S, O'Hare A, Hanicinec M, Dzarasova A, Gorfinkiel J, Benda

[83] J, Mašı□ n Z, Al-Refaie A, Knowles P and Tennyson J 2019 *Atoms* **7** 97
[84] Laporta V, Vialetto L and Guerra V 2022 *Plasma Sources Science and Technology* **31** 054001
[85] McEachran R and Stauffer A 2014 *The European Physical Journal D* **68**
[86] Grofulović M, Alves L L and Guerra V 2016 *Journal of Physics D: Applied Physics* **49** 395207
[87] Ogloblina P, del Caz A T, Guerra V and Alves L L 2020 *Plasma Sources Science and Technology* **29** 015002
[88] Budde M, Dias T C, Vialetto L, Pinhão N, Guerra V and Silva T 2022 *Journal of Physics D: Applied Physics* **55** 445205
[89] Suzuki M, Taniguchi T and Tagashira H 1989 *Journal of Physics D: Applied Physics* **22** 1848–1855
[90] Morgan W L 1991 *Physical Review A* **44** 1677–1681
[91] Morgan W 1991 *IEEE Transactions on Plasma Science* **19** 250–255
[92] Stokes P W, Cocks D G, Brunger M J and White R D 2020 *Plasma Sources Science and Technology* **29** 055009
[93] Kochenderfer M J and Wheeler T A 2019 *Algorithms for optimization* (Mit Press)
[94] Biagi S 1999 *Nuclear Instruments and Methods in Physics Research Section A: Accelerators,*
[95] *Spectrometers, Detectors and Associated Equipment* **421** 234–240
[96] Rabie M and Franck C 2016 *Computer Physics Communications* **203** 268–277
[97] Dias T C, del Caz A T, Alves L L and Guerra V 2023 *Computer Physics Communications* **282** 108554
[98] Hagelaar G J M and Pitchford L C 2005 *Plasma Sources Science and Technology* **14** 722–733
[99] del Caz A T, Guerra V, Gonçalves D, da Silva M L, Marques L, Pinhão N, Pintassilgo C D and
[100] Alves L L 2019 *Plasma Sources Science and Technology* **28** 043001
[101] Stephens J C 2018 *Physics of Plasmas* **25** 103502
[102] Stephens J 2018 *Journal of Physics D: Applied Physics* **51** 125203
[103] Flynn M, Neuber A and Stephens J 2021 A multi-term Boltzmann equation toolset for low temperature plasmas *2021 IEEE Pulsed Power Conference (PPC)* (IEEE)
[104] Flynn M, Neuber A and Stephens J 2021 *Journal of Physics D: Applied Physics* **55** 015201
[105] White R D, Robson R E, Schmidt B and Morrison M A 2003 *Journal of Physics D: Applied Physics* **36** 3125–3131
[106] Flynn M, Agan J, Neuber A and Stephens J Evolution towards a complete set of C_4F_7N cross-sections (manuscript in-preparation)
[107] Biagi database, www.lxcat.net, retrieved on January 24, 2023.
[108] Fortran program, MAGBOLTZ v8.97, S.F. Biagi.
[109] Xiong J, Li X, Wu J, Guo X and Zhao H 2017 *Journal of Physics D: Applied Physics* **50** 445206 [65] Tennyson J 2010 *Physics Reports* **491** 29–76
[110] Dunning T H 1989 *The Journal of Chemical Physics* **90** 1007–1023
[111] Binkley J S, Pople J A and Hehre W J 1980 *Journal of the American Chemical Society* **102** 939–947
[112] 2022 NIST computational chemistry comparison and benchmark database, nist standard reference database number 101 editor: Russell D. Johnson III URL https://cccbdb.nist.gov/elecaff1x.asp

[113] Flynn M, Agan J, Neuber A and Stephens J Generation and optimization of cross-sections for electron-C_4F_7N collisions, *J. Phys. D: Appl. Phys.* **56**, 485207 (2023).
[114] Zhang J, Sinha N, Jiang M, Wang H, Li Y, Antony B and Liu C 2022 *IEEE Transactions on*
[115] *Dielectrics and Electrical Insulation* **29** 1005–1010
[116] Quantemol Ltd. 2022 *Quantemol-EC Release 1.2* available at:
[117] https://www.quantemol.com/software-2/quantemol-ec/qec-release-notes/
[118] Vemulapalli H and Franck C M 2022 *Journal of Physics D: Applied Physics*
[119] Geltman S 1969 *Topics in atomic collision theory* (New York)
[120] Vass M, Egüz E, Chachereau A, Hartmann P, Korolov I, Hösl A, Bošnjaković D, Dujko S, Donkó
[121] Z and Franck C M 2020 *Journal of Physics D: Applied Physics* **54** 035202
[122] Haefliger P and Franck C M 2018 *Review of Scientific Instruments* **89** 023114

APPENDIX A. RGA DATA

The data in this section was collected with an RGA connected to the spark gap switch filled with the mixture shown. The data shows the evolution of M/Q (mass per charge) lines over time at baseline, post-1, post-3, post-5, and post-10 shots. The gray band shows the scan-to-scan variability in that line on baseline shots. For most of the products the scan-to-scan variability was higher than the change over shots or time.

Results for Novec-O2-CO2

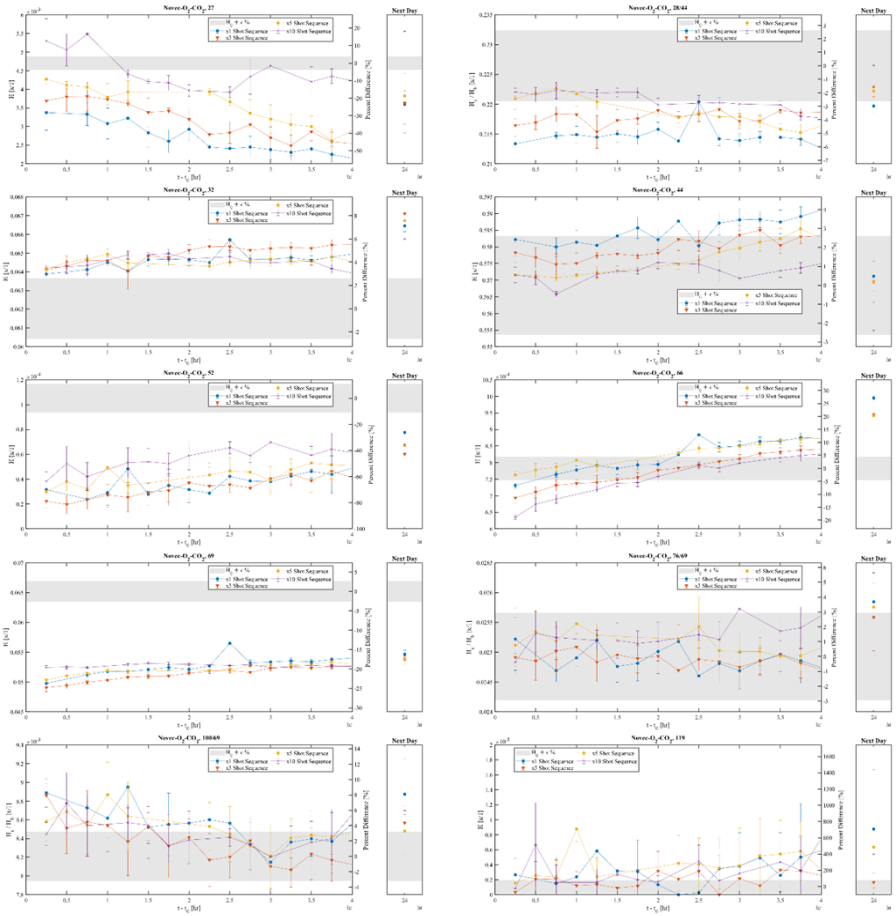

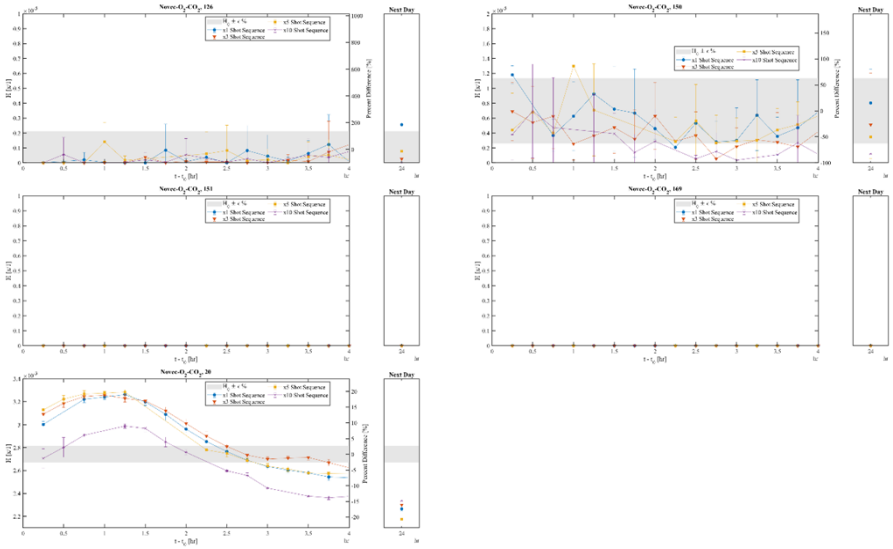

Figure A.1. RGA data for Novec-O2-CO2 mixture at baseline, post-1, post-3, post-5, and post-10 shots.

Results for Novec-CO2

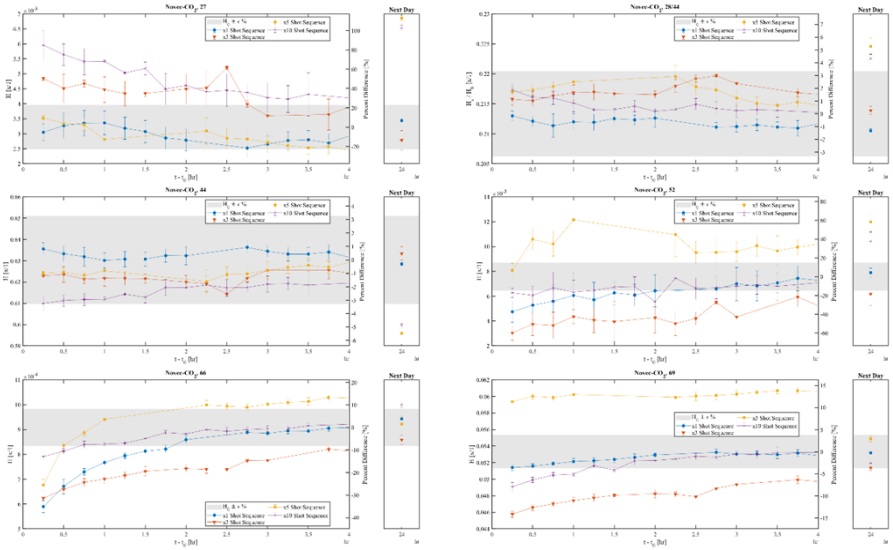

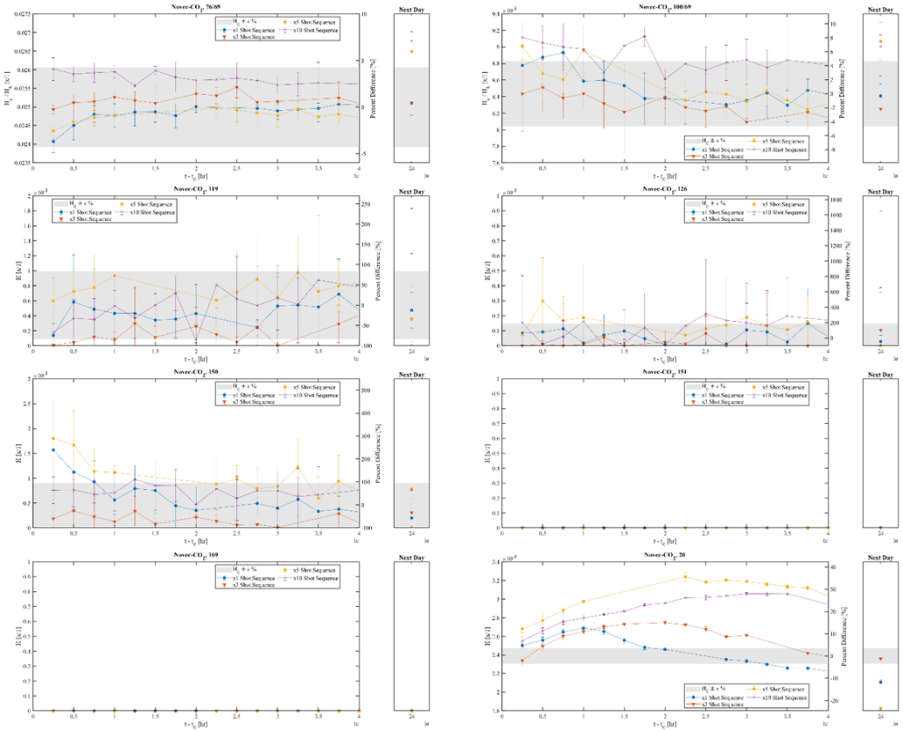

Figure A.2. RGA data for Novec-CO2 mixture at baseline, post-1, post-3, post-5, and post-10 shots.

APPENDIX B. SENSITIVITY TO EXTERNAL CROSS-SECTION SETS

Since the GA procedure includes data from mixtures containing N_2 and CO_2, results likewise depend on the set of cross-sections for N_2 and CO_2 input to the MTBE. The extent to which these externally sourced sets (which, for the Biagi set [62,63], are a combination of experimentally-measured and swarm-optimized curves) over or undercalculate swarm parameters in pure N_2 and CO_2 compared to experimental data may fold a bias within an evolved set. To limit this potential bias, the N_2 and CO_2 cross-sections used for GA optimization (the Biagi set [62,63]) were renormalized (see table B1) such that MTBE calculations in pure N_2 and CO_2 are consistent with the pulsed Townsend data of [75] (the same experimental team as [23] from which the data was selected for optimization).

Swarm parameters in pure N_2 and CO_2 calculated using the same MTBE settings as used in section 3.3 using both original and renormalized cross-section sets are given in figure B.1. Values calculated using the original cross-section sets exceed the data for k_{eff}/N in both N_2 and CO_2 as well as the data for W in CO_2, while those calculated using the sets renormalized via the scales given in table B1 better match the experimental data.

Table B1: Scales applied to create renormalized cross-section sets for N_2 and CO_2. *Table source*: reconfigured from [69].

Collision-type	N_2	CO_2
Attachment	-	0.86
Elastic momentum transfer	1.00	1.08
Vibrational excitation	1.12	1.03
Electronic excitation	1.12	1.03
Ionization	1.12	1.03

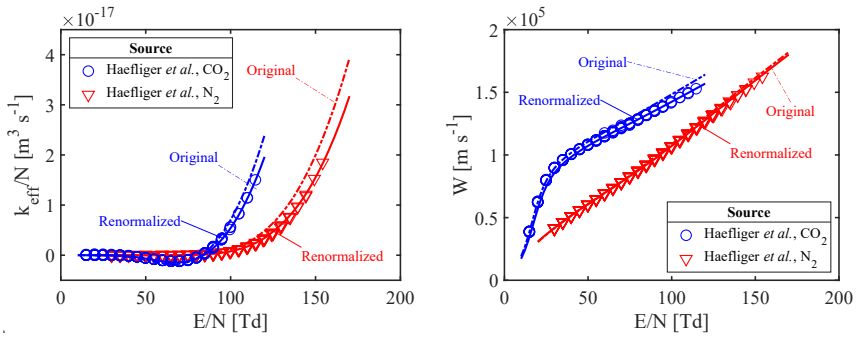

Figure B.1. The impact of cross-section renormalization on swarm parameters calculated in pure N_2 and CO_2. (left) Density-reduced effective ionization rate coefficients and (right) bulk drift velocities in (red) N_2 and (blue) CO_2. (— · —) results calculated using the original sets. (——) are results calculated using the renormalized sets. Markers are the experimental data of Haefliger *et al.* [75]. *Figure source*: [69].

APPENDIX C. CALCULATIONS IN MIXTURES FOR HIGH FIELD STRENGTHS

The cross-section set reported in this work was optimized based on available data for mixtures given in Chachereau *et al.* [23], for which swarms are moderately cool. The ability to calculate swarm parameters for hotter swarms is of note.

Calculations in the 5% C_4F_7N mixtures with N_2 and CO_2 are given in figure C1. Calculations use the same MTBE settings and cross-sections as results reported in section 3. The calculated W and D_LN remain acceptable up to 2,000 Td in both mixtures. For E/N > 1,000 Td, the calculated values of k_{eff}/N for the CO_2 mixture are much larger than the data. Note that, from the data and BOLSIG+ calculations of Vemulapalli and Franck [72], this differing behavior can be attributed to the cross-sections of the carrier gases.

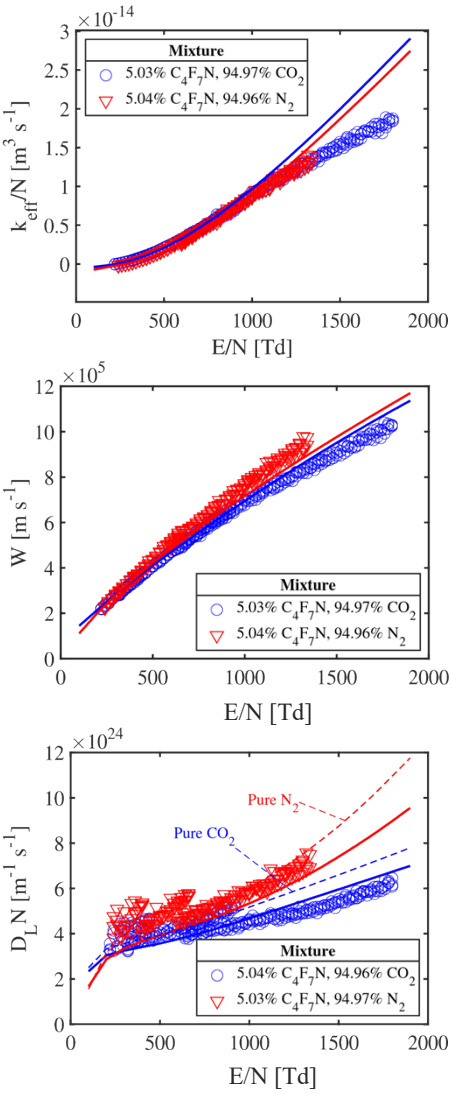

Figure C.1. Calculated rate and transport coefficients in C_4F_7N mixtures with CO_2 and N_2 for high field strengths. Compared with the experimental data of Vemulapalli and Franck [72]. For D_LN, calculations for pure N_2 and CO_2 (- - - -) are also given for comparison. Calculations of k_eff/N and W for the pure gases are very similar to that of the mixtures and are not given.

DISTRIBUTION

Email—Internal

Name	Org.	Sandia Email Address
Technical Library	1911	sanddocs@sandia.gov

Email—External

Name	Company Email Address	Company Name

Hardcopy—Internal

Number of Copies	Name	Org.	Mailstop

Hardcopy—External

Number of Copies	Name	Company Name and Company Mailing Address

This page left blank

Sandia National Laboratories is a multimission laboratory managed and operated by National Technology & Engineering Solutions of Sandia LLC, a wholly owned subsidiary of Honeywell International Inc. for the U.S. Department of Energy's National Nuclear Security Administration under contract DE-NA0003525.